Dear Editor and Referee,

We thank the Referee #1 for the careful and constructive review of our manuscript. The comments and suggestions are of great value to help us to improve the clarity and rigor of the manuscript. We have revised the manuscript and Supplement accordingly. We added 2 new figures in the manuscript, and 21 new figures and 1 table in Supplementary Information.

Especially, we re-did the PMF analysis (compared two factorization methods and three data-treatment approaches), expanded the thermodynamic and kinetic analysis, and revised the descriptions of the particle-size distributions and the 2-D VBS analysis. Kinetic issues are estimated based on Stokes-Einstein equations and validated by Deborah number, while thermodynamics are determined by 2-D-VBS parametrizations and AIOMFAC.

Our point-by-point responses are provided below.

Response to Referee #1

Shen et al. investigate oxidative aging and gas–particle partitioning of cooking emissions using a Go:PAM flow reactor coupled with FIGAERO-CIMS (and supporting measurements). The manuscript argues that secondary organic aerosol (SOA) formation is driven primarily by nucleation/condensation of gas-phase oxidation products rather than by oxidative aging of primary aerosol. The authors further interpret the evolution of composition and volatility using a 2-D VBS framework and Positive Matrix Factorization (PMF), and they propose that smaller molecules approach equilibrium partitioning while larger molecules show non-equilibrium behavior that may reflect kinetic limitations.

The topic is potentially important. Cooking is increasingly recognized as a major contributor to urban primary emissions and to indoor particulate matter exposure, and detailed chemical characterization of cooking-related oxidation and partitioning can be valuable for both air quality and exposure studies.

However, in its current form the manuscript has substantial issues in analysis and presentation that prevent a rigorous evaluation of the main conclusions. My primary

concerns center on the PMF approach/interpretation and the strength of several mechanistic statements. For these reasons, I do not think the manuscript is ready for publication in ACP without major re-analysis and restructuring, and I recommend rejection with encouragement to resubmit after substantial revision.

Response:

Thank you for the careful assessment. We agree that the PMF workflow and factor selection, the interpretation of compositional evolution with increasing OH exposure, and the discussion of gas-particle partitioning required clearer justification. In response, we compared two factorization methods and three data-treatment approaches, reorganized and clarified the PMF factors, expanded the thermodynamic and kinetic analysis, and revised the descriptions of the particle-size distributions and the 2-D VBS analysis. Detailed responses and the corresponding revisions are provided below.

Major comments

1) ***Joint PMF on gas- and particle-phase signals requires stronger justification and validation. The manuscript applies PMF to a combined dataset that includes both gas-phase signals and particle-phase thermal-desorption signals from FIGAERO. While a joint analysis can be feasible in some contexts, it requires clear justification and evidence that the solution reflects chemical/process factors rather than differences in measurement mode, time resolution, and uncertainty structure (real-time inlet vs. integrated filter collection + desorption). As presented, the manuscript does not provide sufficient validation that combining the two phases in a single PMF run yields physically meaningful factors. At minimum, the authors should demonstrate robustness (e.g., compare solutions from gas-only, particle-only, and combined analyses, and show whether the main conclusions are consistent).***

Response: Thank you for this crucial comment. We agree that jointly analyzing gas- and particle-phase signals requires explicit validation because the two measurement modes differ. We therefore compared two factorization methods, ME-2 PMF and MATLAB® NNMF, using three data-treatment approaches: (1) the joint gas- and particle-phase dataset, (2) the particle-phase-only dataset, and (3) a trend-only dataset in which each ion time series was normalized to its maximum. We evaluated each

solution using global metrics, including Q/Q_{exp}, RMSE, and explained absolute variance ($Ratio_{var}$), and time-resolved local metrics, including the summed absolute relative residual and unexplained variation (UEV). Definitions of these metrics are briefly provided below and described in detail in Section S4 of Supplement S1.

$$Q = \sum_{j=1}^{m}\sum_{i=1}^{n}\left(\frac{E_{ij}}{\sigma_{ij}}\right)^2 \qquad Q_{exp} = n \times m - p \times (p + m)$$

$$RMSE = \sqrt{\frac{\sum_{j=1}^{m}\sum_{i=1}^{n}(E_{ij})^2}{n \times m}}$$

$$Ratio_{var} = \frac{\sum_{ij}|R_{ij} - \overline{X_i}|}{\sum_{ij}|R_{ij} - \overline{X_i}|}$$

$$\text{Sum relative residual}_i = \frac{\sum_j R_{ij} - X_{ij}}{\sum_j |X_{ij}|}$$

$$\text{absolute relative residual}_i = \frac{\sum_j |R_{ij} - X_{ij}|}{\sum_j |X_{ij}|}$$

$$UEV_i = \frac{\sum_j |e_{ij}/\sigma_{ij}|}{\sum_j |X_{ij}/\sigma_{ij}|}$$

Candidate solutions were required to have UEV <25% and Q/Q_{exp} close to 1. We first identified turning points in Q/Q_{exp}, RMSE, and $Ratio_{var}$, where improvement became substantially slower as the factor number increased. We then examined whether adding factors around these turning points significantly improved the time-resolved local metrics. Finally, we assessed the physical interpretability of the factor thermograms. The same global and local metrics were used to compare the factorization and data-treatment methods. Pairwise spectral contrast angles (θ), calculated by treating each factor spectrum as a vector in species-concentration space, were used to evaluate factor similarity; angles were required to exceed 30°.

MATLAB® NNMF showed lower RMSE and higher $Ratio_{var}$, particularly below 10 factors, but it does not explicitly account for measurement uncertainty. When the uncertainty-weighted Q/Q_{exp} metric and local residuals were considered, ME-2 PMF performed better. The two methods showed comparable bias only for the normalized time-series dataset, which was intended mainly to extract temporal evolution patterns and volatility distributions. For ME-2 PMF, the full time-series dataset performed slightly better than the particle-phase-only dataset and clearly better than the normalized dataset (Figures S4.7-9). By contrast, NNMF favored the normalized full time series, especially during the primary-emission period (Figures S4.4-6). Based on

the ME-2 PMF results for the full time series, we selected the 13-factor solution because adding more factors did not substantially improve the global metrics or the local fits for most time periods and detected species. All pairwise spectral contrast angles in the 13-factor solution were >30°, with a minimum of 35°, indicating limited collinearity among the factors (Figure S4.13).

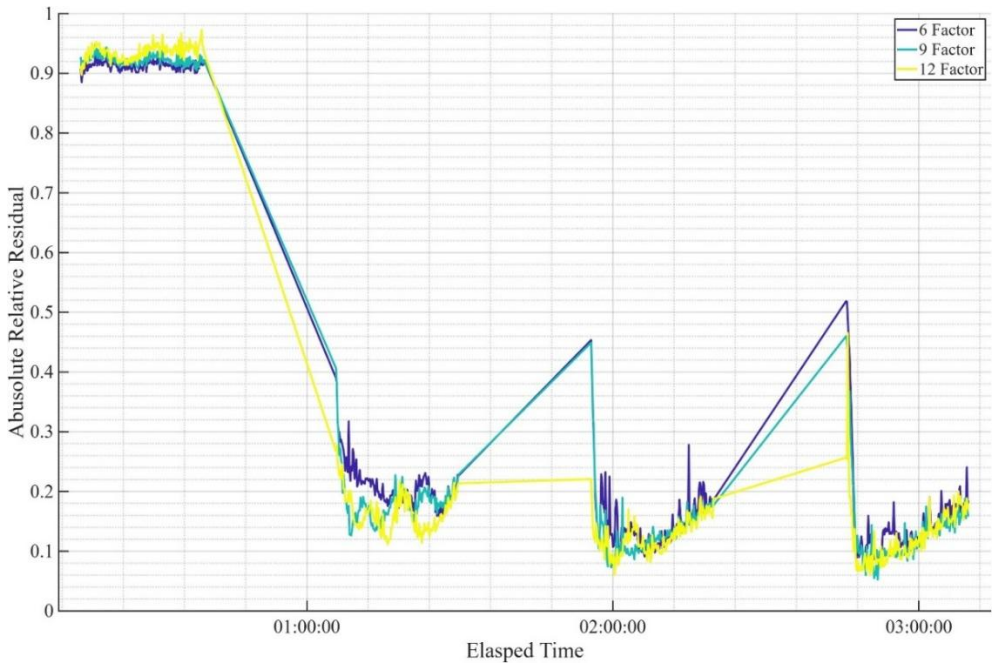

Figure S4.4 Detailed absolute relative residual time series of factorization results of particle-phase only data utilizing MATLAB NNMF at factor number 6, 9 and 12 which are selected to be right at “turning points”

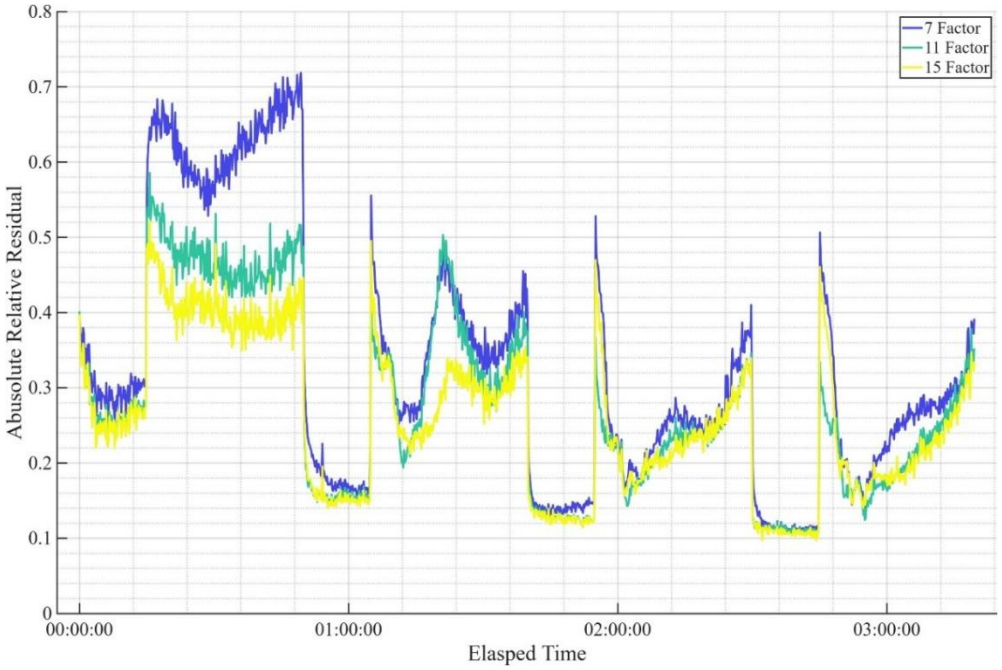

Figure S4.5 Detailed absolute relative residual time series of factorization results of normalized full time-series data utilizing MATLAB NNMF at factor number 7,11 and 15 which are selected to be right at "turning points"

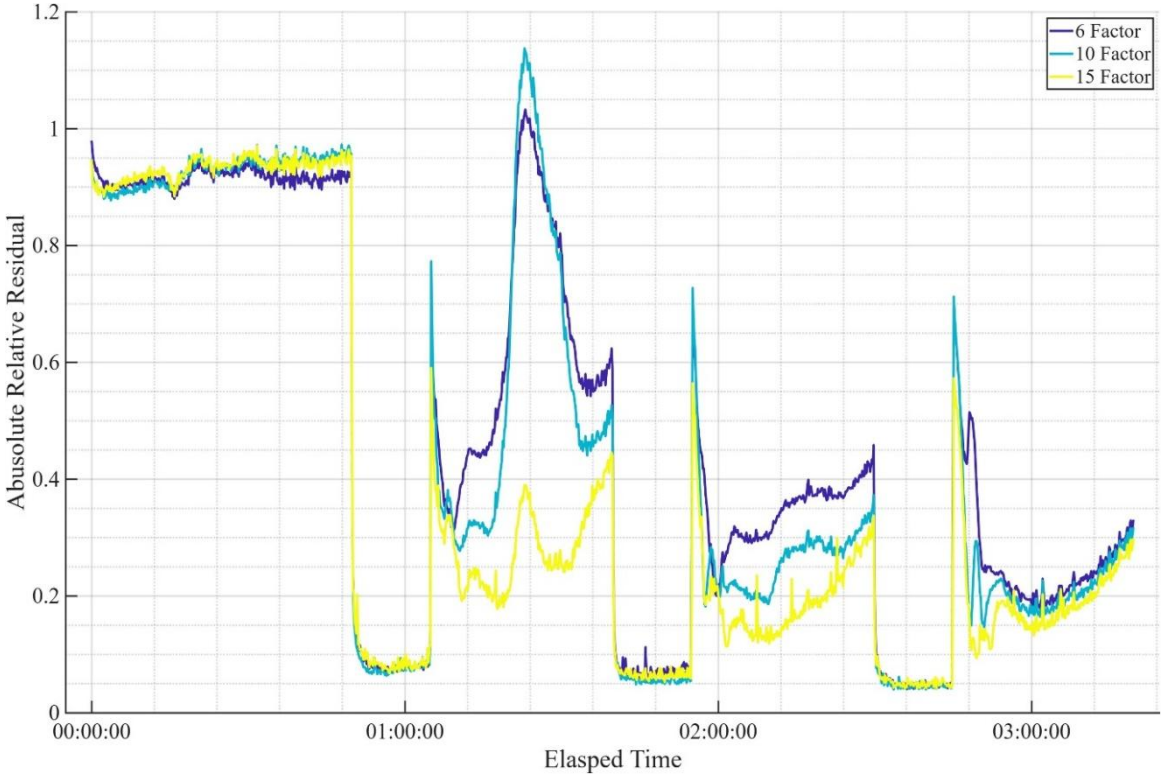

Figure S4.6 Detailed absolute relative residual time series of factorization results of full time-series data utilizing MATLAB NNMF at factor number 6,10 and 15 which are selected to be right at "turning points"

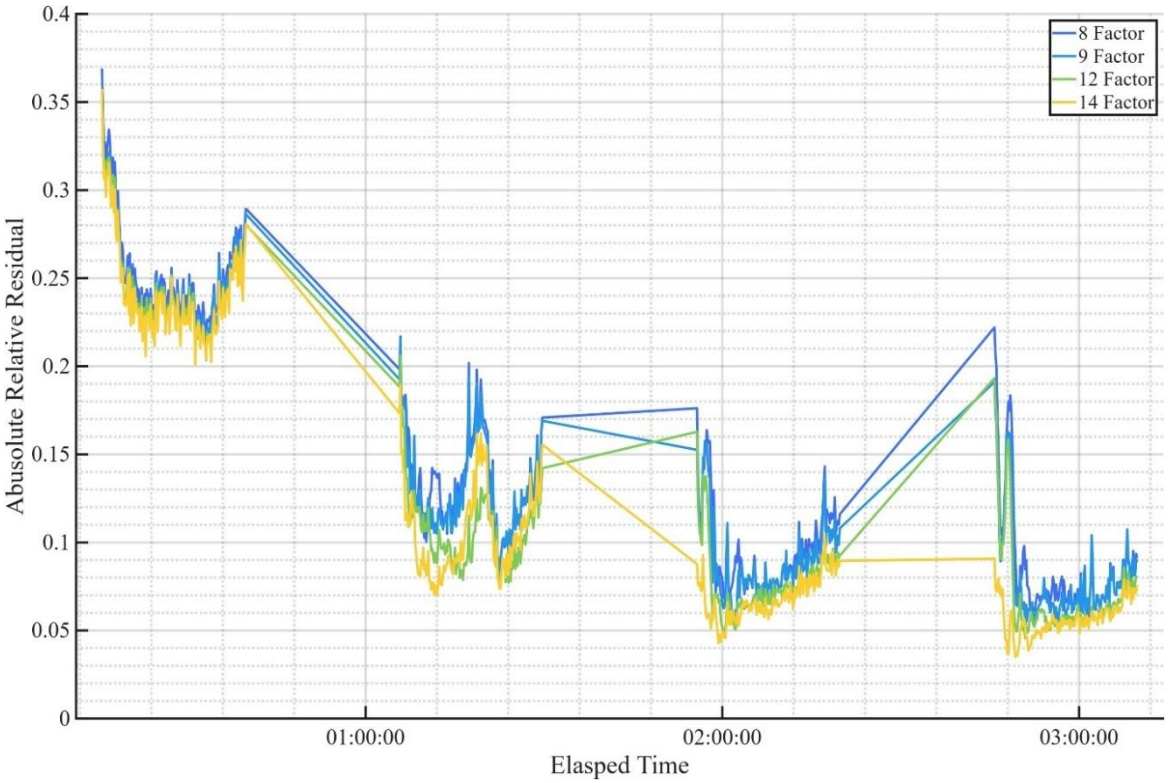

Figure S4.7 Detailed absolute relative residual time series of factorization results of particle-phase only data utilizing ME-2 PMF with 8,9,12 and 14 factors which are selected to be right at "turning points"

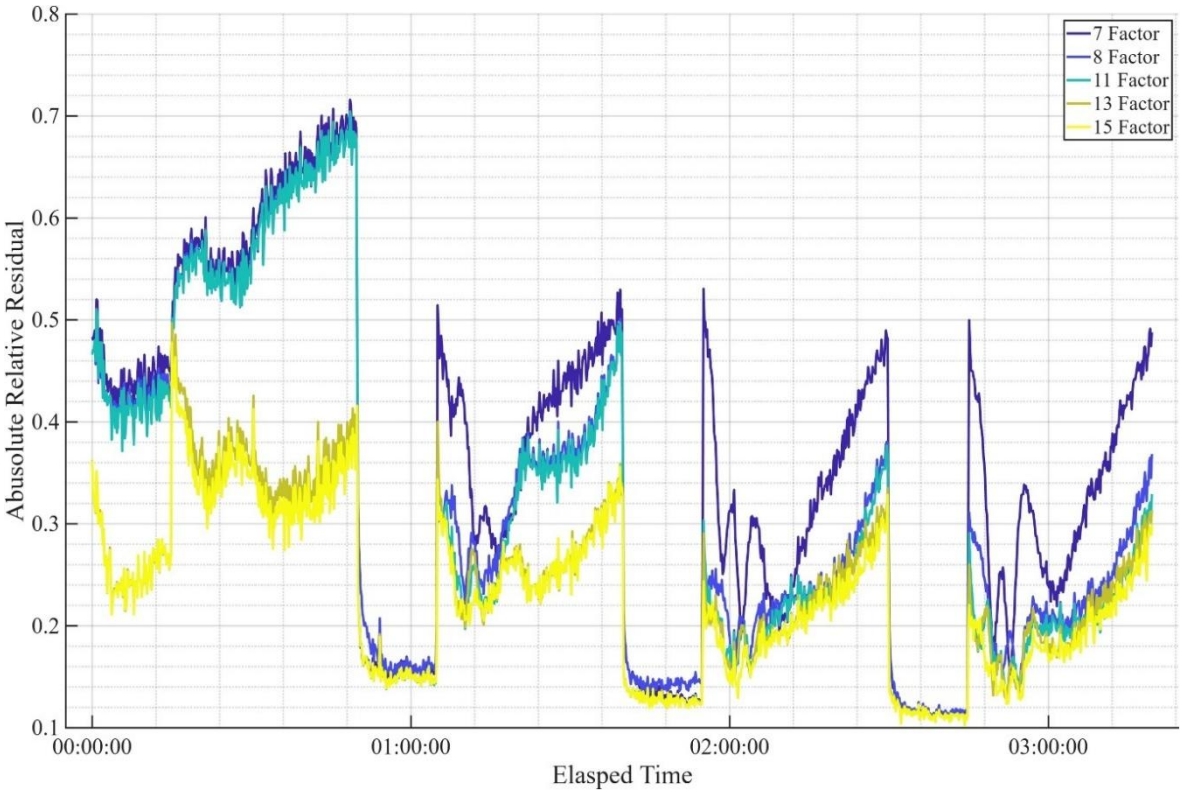

Figure S4.8 Detailed absolute relative residual time series of factorization results of normalized full time-series data utilizing ME-2 PMF with 7,8,11,13 and 15 factors which are selected to be right at "turning points"

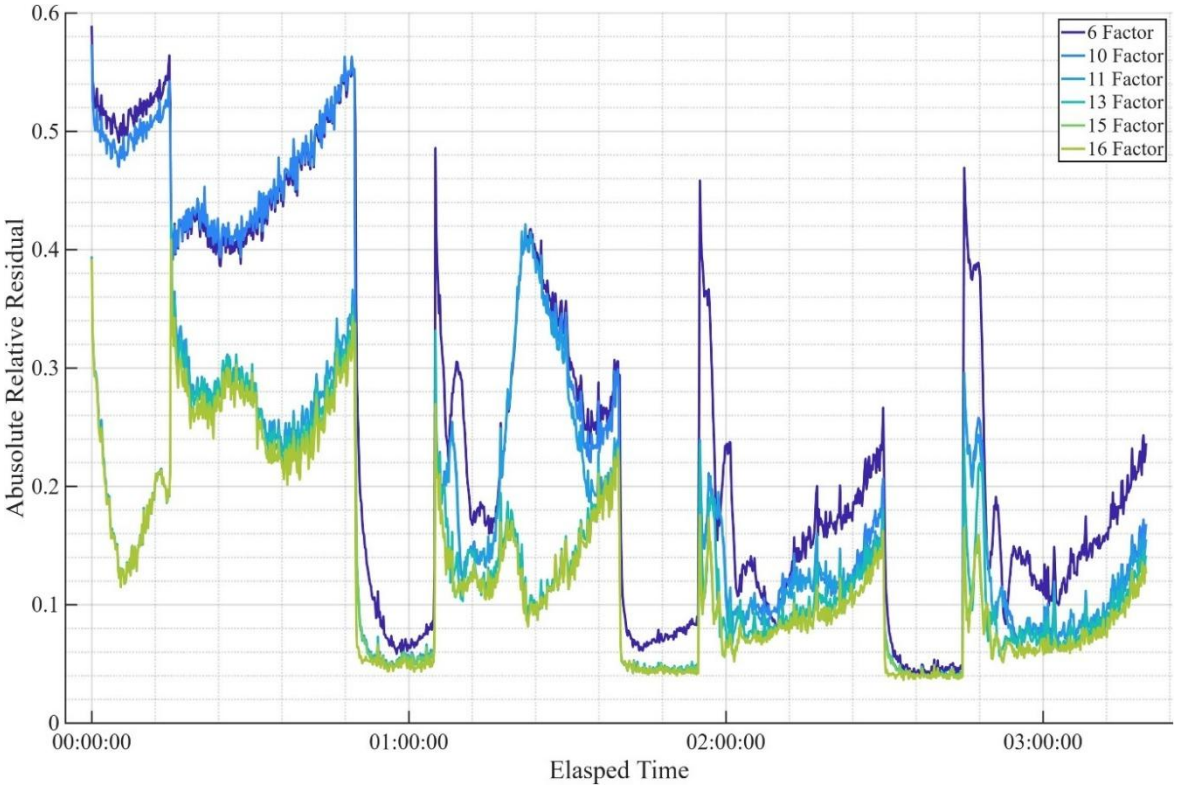

Figure S4.9 Detailed absolute relative residual time series of factorization results of full time series data utilizing ME-2 PMF with 6,10,11,13,15 and 16 factors which are selected to be right at "turning points"

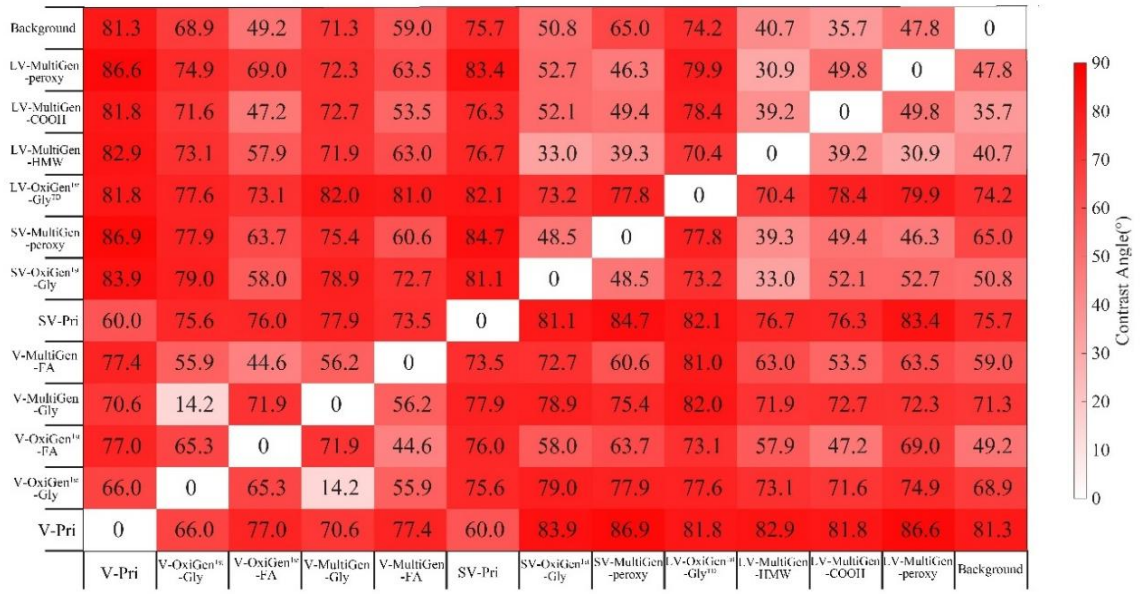

Figure S4.13 Contrast angle in degree between factors resolved by ME-2 PMF

We therefore selected ME-2 PMF with the full time-series dataset as the main analysis and retained the 13-factor solution as the most interpretable result. The detailed comparison of factorization methods, data-treatment methods, and factor-number selection is provided in Section S4 of Supplement S1.

The corresponding revisions in Section 2.4 and Section S4 of Supplement S1 read:

"To evaluate whether the joint gas- and particle-phase analysis yielded a robust solution, we compared ME-2 PMF and MATLAB® NNMF using three input matrices: the full gas- and particle-phase time series, the particle-phase-only dataset, and a trend-only dataset in which each ion time series was normalized to its maximum. The solutions were evaluated using Q/Q_{exp}, RMSE, explained absolute variance ($Ratio_{var}$), time-resolved summed absolute relative residuals, and unexplained variation (UEV)."

"Candidate solutions were required to have UEV <25% and Q/Q_{exp} close to 1. Factor-number turning points were first identified from Q/Q_{exp}, RMSE, and Ratiovar. We then examined changes in the time-resolved local metrics and the physical interpretability of the factor thermograms. Pairwise spectral contrast angles were additionally used to evaluate factor similarity."

"ME-2 PMF with the full time-series dataset was selected as the main analysis because it performed better when measurement uncertainty and local residuals were considered. The 13-factor solution was retained because adding further factors did not substantially improve the global or local diagnostics. All pairwise spectral contrast angles were >30°, with a minimum of 35°, indicating limited collinearity among the retained factors."

2) ***The PMF results are presented in an overly descriptive manner, making the factor interpretation difficult to follow and limiting scientific insight. Section 3.3 reports 13 factors and discusses their dominant ions/tracer-like species, but the factors are not assigned intuitive labels (source/process-oriented) and the narrative does not clearly articulate what each factor represents in a way that readers can track across the manuscript. As a result, it is difficult to understand why resolving these factors is important, how they connect to the SOA formation stages, and what new chemistry/mechanistic insight is gained beyond listing factor constituents. The structure of Section 3.3 also makes the discussion hard to follow; additional organization (e.g., subheadings and grouping factors by interpretation) would greatly improve clarity.***

Response: Thank you for this suggestion. We revised Section 3.3 and Section S4 of Supplement S1 to group the factors by volatility, composition, and their evolution with increasing OH exposure (Figure 3). The factor with an implausible thermogram containing three separated peaks is classified as a background factor (light yellow). The remaining factors are first grouped as volatile (V; predominantly gas phase), semi-volatile (SV; abundant in both gas and particle phases), or low-volatility (LV; predominantly particle phase). The suffixes describe composition and oxidation-stage behavior. V-Pri and SV-Pri are most abundant in primary emissions and decrease with OH exposure; V-Pri is dominated by lower-molecular-weight oxygenated compounds, including short-chain carboxylic acids and their derivatives, whereas SV-Pri contains larger compounds, including long-chain fatty acids such as palmitic and oleic acids. V-OxiGen1st-FA represents first-generation products from long-chain fatty-acid oxidation. V-OxiGen^{1st}-Gly, V-OxiGen^{1st}-FA, SV-OxiGen^{1st}, and LV-OxiGen^{1st}-GlyTD peak at intermediate OH exposure. The glycerol-structure-related V-OxiGen^{1st}-Gly and LV-OxiGen^{1st}-GlyTD factors peak at lower exposure than the fatty-acid-related V-OxiGen^{1st}-FA and SV-OxiGen^{1st} factors. The multi-generation oxidation-product group includes V-MultiGen-Gly, V-MultiGen-FA, SV-MultiGen-peroxy, LV-MultiGen-HMW, LV-MultiGen-COOH, and LV-MultiGen-peroxy, which are most abundant at the highest OH exposures. V-MultiGen-Gly and LV-MultiGen-HMW tend toward a steady state at the highest exposure and retain features related to cooking-oil structures, whereas the other multi-generation factors are more oxidized, are associated with scission products of oil-derived structures, and continue to increase. Evidence on factor assignments are shown in Figure S4.15 that depict gas-particle partitioning coefficients K_p of each factor, and Figures S4.16-18 showing relative abundance of factors at different OH exposure. These revisions make the factor roles and their connection to the oxidation sequence easier to follow.

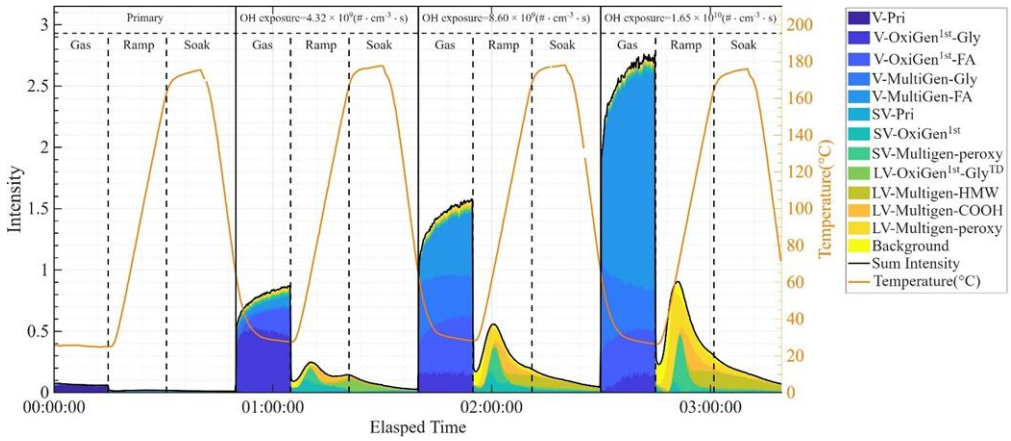

Figure 3. Time series of the classified ME-2 PMF factors derived from FIGAERO-I-CIMS data.

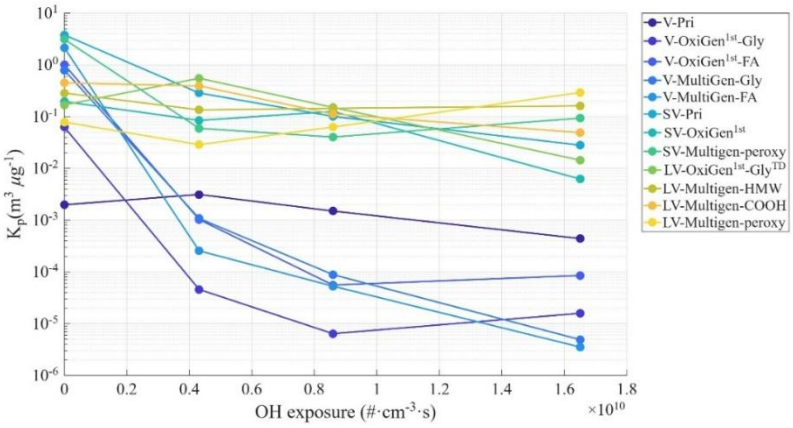

Figure S4.15 Evolution of factors' gas-particle partitioning coefficient K_p with enhancement of OH exposure during oxidation process and classification by its volatility

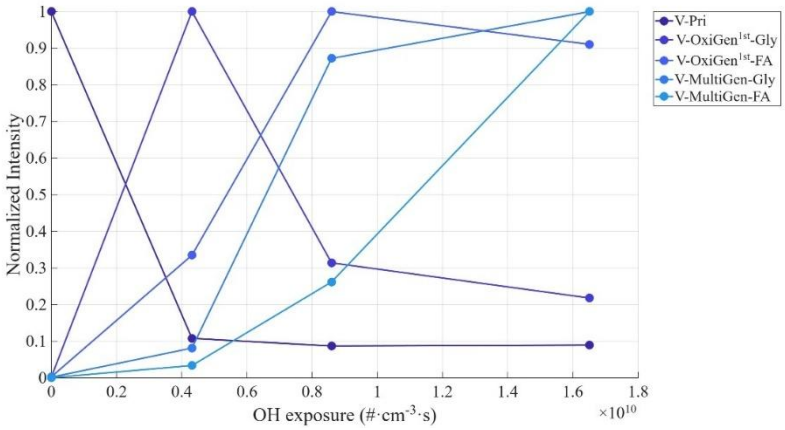

Figure S4.16 Evolution of factors' average relative intensity classified as volatile factor (only abundant in gas phase) with enhancement of OH exposure during oxidation process

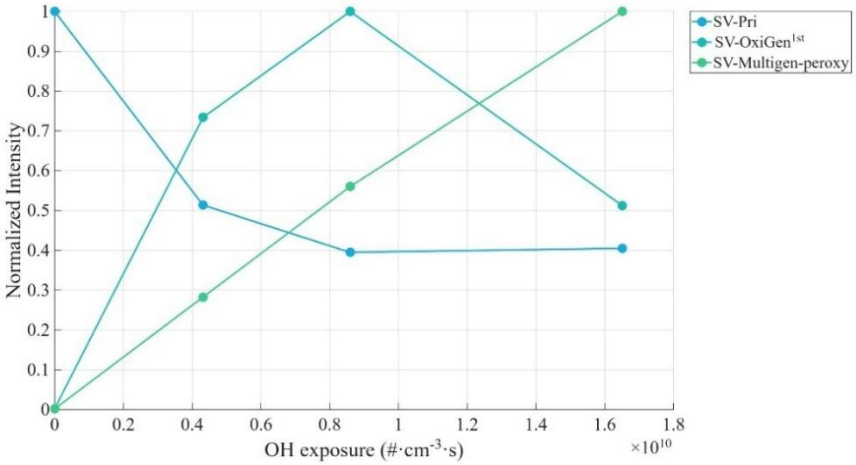

Figure S4.17 Evolution of factors' average relative intensity classified as semi-volatile factor (both abundant in gas phase and aerosol phase) with enhancement of OH exposure during oxidation process

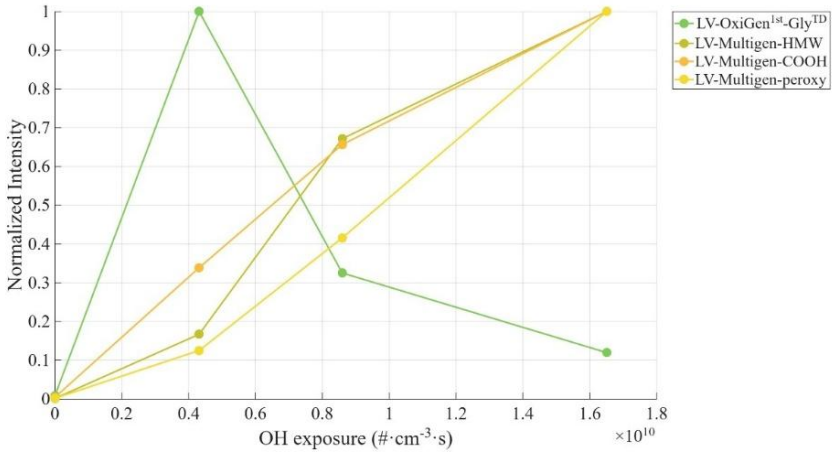

Figure S4.18 Evolution of factors' average relative intensity classified as low-volatile factor (only abundant in aerosol phase) with enhancement of OH exposure during oxidation process

The revised factor-grouping description in Section 3.3 reads:

"The factor with an implausible thermogram containing three separated peaks was classified as a background factor. The remaining factors were first grouped as volatile (V; predominantly gas phase), semi-volatile (SV; abundant in both gas and particle phases), or low-volatility (LV; predominantly particle phase). The suffixes describe the compositional interpretation and the oxidation stage at which each factor is most abundant."

"V-Pri and SV-Pri are most abundant in primary emissions and decrease with OH exposure. The first-generation group includes V-OxiGen1st-Gly, V-OxiGen1st-FA, SV-OxiGen1st, and LV-OxiGen1st-GlyTD, which peak at intermediate OH exposure. The

multi-generation group includes V-MultiGen-Gly, V-MultiGen-FA, SV-MultiGen-peroxy, LV-MultiGen-HMW, LV-MultiGen-COOH, and LV-MultiGen-peroxy, which are most abundant at the highest OH exposures. This grouping connects factor volatility and composition with the observed oxidation sequence."

3) ***Mechanistic attribution of non-equilibrium partitioning to particle-phase diffusion / mass-transfer limitations is overstated relative to the evidence shown. The abstract and conclusions present particle-phase diffusion/mass-transfer limitation as a key explanation for kinetic limitations in gas–particle partitioning of larger molecules. In the main text (Section 3.4), this appears to be one proposed explanation among others rather than a demonstrated mechanism. The manuscript does not provide quantitative constraints (e.g., phase state/viscosity proxies, diffusion coefficients or mixing timescales, uptake/accommodation considerations, sensitivity analyses) that would allow the reader to evaluate whether diffusion or mass-transfer limitations are sufficient to explain the observed deviations. Without such evidence, the current wording reads as a conclusion stronger than what is actually supported, and should be reconsidered.***

Response: We agree that the previous attribution to particle-phase diffusion limitations was too strong and lacked conclusive evidence. We expanded the thermodynamic and kinetic analysis in Section 3.4 and Section S5 of Supplement S1 using AIOMFAC for activity coefficients, 2-D VBS parameterizations for volatility (Donahue et al., 2011, doi: 10.5194/acp-11-3303-2011; Li et al., 2016, doi: 10.5194/acp-16-3327-2016), the viscosity parameterization of DeRieux et al. (2018, doi: 10.5194/acp-18-6331-2018), and kinetic parameterizations on gas-phase diffusion, (Evoy et al.2019, DOI: 10.5194/acp-19-10073-2019;Knopf et al., 2024, doi: 10.5194/acp-24-3445-2024; Shiraiwa and Pöschl, 2021, doi: 10.5194/acp-21-1565-2021). We also evaluated the applicability of Fickian diffusion and the fractional Stokes-Einstein relationship between viscosity and diffusion kinetics (DOI: 10.1139/cjc-2021-0187).

Detailed gas-particle partitioning mechanism and estimation methods are shown below. Analysis of volatility and gas-particle partitioning thermodynamics of organic compounds detected by FIGAERO-CIMS are processed by gas-phase and aerosol-

phase concentration. Direct gas-particle partitioning characteristics are shown by particle-phase fraction F_p, shown in Equation S5.1:

$$F_{p,i} = \frac{c_{p,i}}{c_{g,i}+c_{p,i}} \quad \text{S5.1}$$

In Equation R5.1, $c_{p,i}$ stands for particle phase concentration of substance i, $c_{g,i}$ means gas phase concentration. Partitioning coefficient K_p, considering influence organic aerosol as substrate of compound i, is defined in Equation S5.2：

$$K_{p,i} = \frac{c_{p,i}/c_p}{c_{g,i}} \quad \text{S5.2}$$

In Equation R5.2, c_p means total particle concentration. F_p and $K_{p,i}$ can be directly derived from FIGAERO-CIMS gas-particle simultaneous detection of certain compound (including iodide-adduct ion $[RI^-]$ or proton-extraction ion $[R\text{-}H]^-$ corresponding to species R), and aerosol mass concentration, shown in Equation S5.3-5.4:

$$(F_{p,i})_{exp} = \frac{\overline{([RI^-]/[I^-])}_{aero}\cdot Q_{TD}\cdot \Delta t_{TD}}{[\overline{([RI^-]/[I^-])}_{gas}\cdot Q_{col}\cdot \Delta t_{col}+\overline{([RI^-]/[I^-])}_{aero}\cdot Q_{TD}\cdot \Delta t_{TD}]} \quad \text{S5.3}$$

$$(K_{p,i})_{exp} = \frac{\overline{([RI^-]/[I^-])}_{aero}\cdot Q_{TD}\cdot \Delta t_{TD}}{[\overline{([RI^-]/[I^-])}_{gas}\cdot Q_{col}\cdot \Delta t_{col}]\cdot \overline{c_{p,SMPS}}} \quad \text{S5.4}$$

In Eqs. S5.3-5.4, Δt_{TD} and Q_{TD} means, particle-phase thermal desorption duration and flow rate, Δt_{col} and Q_{col} stand for collection duration and flow rate, $c_{p,SMPS}$ means average SMPS-measure particle concentration during particle collection period of FIGAERO-CIMS measurements. Eqs. S5.3-5.4 can be used to classify PMF factor from volatility angle by substituting intensity of certain compound ($[RI^-]/[I^-]$) with the intensity of PMF-extracted factors.

Absorptive partitioning mechanisms are adopted in gas-particle partitioning thermodynamic characteristics in cooking POA and SOA, as organic compounds existing in aerosol phase composite of a liquid-organic-solution-like or semi-solid-like phase state. Considering the mechanism of absorptive partitioning, F_p is related to mass of total particle phase organics c_{OM}, shown in Equation S5.5, while K_p only depends on properties of compound i and particle phase composition. Assuming gas-particle

partitioning of component i reaches equilibrium, partitioning coefficient $K_{p,i}$ is determined by its volatility and composition of aerosol matrix, as shown in Equation S5.6:

$$(F_{p,i})_{theo} = \left(1 + \frac{c^*}{c_{OM}}\right)^{-1} \quad \text{S5.5}$$

$$(K_{p,i})_{theo} = \frac{RTf_{OM}}{\overline{MW_{OM}} p^0_{L,i} \xi_i} \quad \text{S5.6}$$

In Eq. S5.6, f_{OM} means mass fraction of organic compounds in aerosols, which equals to 1 in this study as inorganic aerosols are rarely formed in cooking aerosols. MW_{OM} stands for average molecular weight among all species in organic aerosol. $p^0_{L,i}$ means saturated vapor pressure of component i over liquid pure component surface. ξ_i means activity coefficient in particle phase. Assuming ξ_i close to unity, the volatility of component i can be determined from gas-particle partitioning of component. If we are able to classify the exact structure from possible reaction pathways during oxidation of utilize estimation method of volatility from corresponding compound detected by CIMS such as SIMPOL.We could also adopt 2-D VBS approach shown in Section S3 to calculate volatility, activity coefficients and K_p of certain species, which may lead to larger bias due to its simple parameterization. Volatility of species i can be also determined by thermogram from thermal desorption measurements of particle phase according to methods, which may be more accurate than partitioning method due to possible interference of FIAGERO collection such as thermal decomposition and matrix effect of the PTFE filter. Activity coefficient ξ_i can be determined by utilizing 2-D-VBS parametrization or using group-contribution model. In this study, we utilized AIOMFAC-web(https://aiomfac.lab.mcgill.ca/), choosing concentration of 50 most abundant compounds in aerosol at each oxidative exposure, treat residual compounds as same molecule with composition equal to average composition of these compounds, to resolve the activity coefficients of most abundant compounds. We also determine the activity of these most abundant compounds to ensure whether liquid-liquid separation occurs in cooking aerosols.

Kelvin effects and influence on gas-particle partitioning are also estimated as it

would be essential in particles with diameter ~10nm. Influence of kelvin effect on partitioning are shown in Equation S5.7. Kelvin effect on gas-particle partitioning is linked to diameter d_p and surface tension σ_i (set to 0.05N·s^{-2}).

$$p_i^* = \xi_i x_i p_{L,i}^0 / Ke_i = \xi_i x_i p_{L,i}^0 exp(\frac{4V_{m,i}\sigma_i}{RTd_p}) \quad \text{S5.7}$$

Gas-particle partitioning of organic species may not reach equilibrium due to kinetic limitations in transportations of molecules in gas phase, at surface or in aerosol phase. Gas-particle partitioning kinetics consist of gas phase diffusion, surface accommodation and particle-phase diffusion processes. Kinetics are characterized by gas-phase diffusion coefficient $D_{g,i}$, surface accommodation coefficient α, particle-phase diffusion coefficient $D_{p,i}$, and corresponding characteristic time scales τ_g, τ_{surf} and τ_p. Gas phase diffusion coefficient of species i in real atmosphere are calculated based on elemental composition of selected species from Fuller's method:

$$D_{g,i} = \frac{1.0868 \times T^{1.75}}{p \cdot \sqrt[3]{m(i,A)} \cdot (\sqrt[3]{V_A} + \sqrt[3]{V_i})^2} \quad \text{S5.8}$$

In equation S5.8, $D_{g,i}$ is in cm^2 s^{-1}, T and p stand for atmospheric temperature and pressure in Kelvin and Torr, m(i,A) means reduced molar mass of species i and ambient air in g/mol, V_i and V_A are molecular diffusion volume of ambient air and selected species i that are directly derived from elemental composition of molecules. Most organic species involved in gas-particle partitioning have diffusion coefficient within 10^{-2} to 10^{-1} cm^2 s^{-1} level utilizing Eq. S5.8. Diffusion time scale corresponding to gas-phase diffusion τ_g are inverse proportional to the gas-phase diffusion rate constant $k_{gp,i}$, determined by Equations S5.9-5.12:

$$\tau_{g,i} = 1/k_{gp,i} \quad \text{S5.9}$$

$$k_{gp,i} = \sum_p 4\pi D_{g,i} r_p N_p \beta \quad \text{S5.10}$$

$$\beta = \frac{0.75\alpha(1+Kn)}{Kn^2 + Kn + 0.283Kn\alpha + 0.75\alpha} \quad \text{S5.11}$$

$$Kn = \frac{3D_{g,i}}{\omega r_p} \quad \text{S5.12}$$

In Equations S5.9-5.12, r_p is particle radius, d_p is diameter and N_p is particle

number concentration at certain diameter range, measured by SMPS; β is correction factor adjusting surface accommodation related to Knudsen number Kn, ω is mean thermal velocity of species i. In Eqs. S5.8-5.11, the ability of species i to adsorb onto particle surface has been accounted by factor β. Till now, mass accommodation coefficient α has been measured by well-designed thermodynamic experiments, while their still lacks efficient parametrization methods to estimate mass accommodation coefficients. In this study, we varied mass accommodation coefficients in an atmospheric-reality-relevant range (from 0.0001 to 1), to observe the effect of variating surface accommodation, thus approaching real α in aerosol phase. An effective mass accommodation coefficient $\alpha_{eff}(x)$ as function of penetration depth x into aerosol phase, thus accounting for near-surface-bulk diffusion based on kinetic modeling of cross-surface mass-transfer processes are shown in Equation S5.13, where x is set to be $d_p/10$:

$$\alpha_{eff} = \alpha \frac{1}{1+\frac{\alpha\omega C^0}{4D_{p,i}\rho_p}x} \qquad \text{S5.13}$$

Diffusion coefficient of species i, $D_{p,I}$, are refined by particle phase viscosity ν. The Stokes-Einstein relation of deriving $D_{p,i}$ from particle phase viscosity are shown in Equation S5.14:

$$D_{p,i} = \frac{kT}{6\pi a\nu} \qquad \text{S5.14}$$

In Eq. S5.14, k is Boltzmann constant, T is particle-phase temperature, a means effective molecular diameter in molecular diffusion, or so-called 'hydrodynamic radius/radii', which are derived based on estimation utilizing molecular weight(https://www.fidabio.com/molecular-weight-to-size-protein-radius-calculator). The effective molecular diameter of organic compounds in atmospheric organic aerosols are at the level of several Å.

Parametrization of particle-phase viscosity ν are estimated by several methods. Viscosity generated from AIOMFAC-web output utilizing AIOMFAC-VISC model are selected as one of the reference viscosities. Modified Vogel–Tammann–Fulcher method links glass transition temperature T_g of particle bulk to viscosity at certain temperature,

as shown in Equation S5.15:

$$\log_{10}\nu = \log_{10}\nu_{\infty} + 0.434\frac{T_0 D}{T-T_0} \quad \text{S5.15}$$

In Eq. S5.15, $\nu_{\infty}=10^{-5}$ Pa·s means viscosity limits when temperature tends to infinity, T stands for ambient temperature, T_0 means Vogel temperature that derived from glass-transition temperature, D=10 means sensitivity of viscosity to temperature changes. Vogel temperature can be determined in Equation S5.16 assuming viscosity to be 10^{12} Pa when temperature reaches T_g:

$$T_0 = \frac{39.17 T_g}{D+39.17} \quad \text{S5.16}$$

For T_g parameterization, several methods are utilized and compared in this study. A simple 2-D-VBS-space based parametrization method introduced by Derieux et al. are adopted to acquire a comparable result to 2-D-VBS-based thermodynamics, where T_g (K)can be directly derived from elemental composition, shown in Equation S5.16. Parameters used in Eq. S5.17 are shown in Table S5.1

$$T_g(K) = b_C \cdot (n_C^0 + ln(n_C)) + b_H \cdot ln(n_H) + b_{CH} \cdot ln(n_C) \cdot ln(n_H) + b_O \cdot ln(n_O) + b_{CO} \cdot ln(n_C) \cdot ln(n_O) \quad \text{R5.17}$$

Table S5.1 Parameters used in glass transition temperature parametrization method developed by Derieux et al., 2018

Elemental composition	n_C^0	b_C	b_H	b_O	b_{CH}	b_{CO}
CH	1.96	61.99	-133.33	28.74	-	-
CHO	12.13	10.95	-41.82	21.61	118.96	-24.38

A machine learning method tgBoost for retrieving glass transition temperature from molecular structure represented by SMILES string are utilized in this study as reference. Over 130000 compounds containing CHONS elements are chosen from NCI database (https://cactus.nci.nih.gov/ncidb2.2/) and entered the tgBoost website to achieve their glass-transition temperatures of the full database(https://azoth-frontend-

lb-9735005.us-west-2.elb.amazonaws.com/). The estimated T_g of species detected by CIMS are set to mean T_g of compounds from tgBoost with same elemental compositions. tgBoost result in a lower T_g than other parameterization methods in estimating multifunctional compounds such as dicarboxylic acids and peroxides.

Another simple T_g estimation method is empirical linear estimation between T_g and melting point T_m. The relation is shown in equation S5.18:

$$T_g = 0.70085 \cdot T_m \quad \text{S5.18}$$

T_g of bulk organic aerosols are determined utilizing Gordon-Taylor equation. Assuming the Gordon-Taylor constant to be equals to 1, resulting in a mass-fraction(w_i)-weighted average of single compounds, shown in Equation S5.19. $T_{g,bulk}$ would be used in Eqs. S5.18-5.19 to determine diffusion coefficient of species in bulk aerosols

$$T_{g,bulk} = \sum_i T_{g,i} w_i \quad \text{S5.19}$$

In real-world diffusion processes within organic aerosols, viscosity would lead to bias away from standard Stokes-Einstein relations, especially for small molecules in viscous matrices, because composition and molecular structure heterogeneity within semi-solid and glassy aerosols lead to internal stress and thus confine transportation of particle compounds. Fractional Stokes-Einstein relations are introduced to close the gap, where $D_{p,i}$ is inversely proportional to ξth power of viscosity rather than viscosity itself, shown in Equation S5.20:

$$D_{p,i} = D_c \left(\frac{\nu}{\nu_c}\right)^{\xi} \quad \text{S5.20}$$

In Eq. S5.20, ξ are the fractional power index, set to be 0.93 recommended by Evoy et al.; D_c and ν_c means crossover diffusion coefficients, while ν_c is set to 10^{-3} Pa·s. Deborah number De, defined as the ratio of characteristic relaxation time τ_ν to the characteristic diffusion time τ_D, are also introduced to ensure whether diffusion in particle phase bias from Stokes-Einstein significantly as shown in Equation S5.21:

$$De = \frac{D_{p,i} \nu M_i}{\rho_i^0 r^2 RT} \quad \text{S5.21}$$

In Equation S5.21, M_i means molecular weight of species i, ρ_i^0 means density of pure species i, r means diameter of the particle. Deborah number De<<1 indicates diffusion mechanism close to Stokes-Einstein equation, while De>>1 showing diffusion characteristic bias significantly from Stokes-Einstein equation. Maxwell-Stefan diffusion theory is used characterize diffusion in presence of internal stress. The diffusion coefficient between S-E diffusion and M-S diffusion is related to partial deviate of activity coefficients shown in Equation S5.22:

$$D_{p,i}(MS) = D_{p,i}(SE) \cdot (1 + \frac{1}{x_i(\frac{\partial \ln \xi_i}{x_i})_{T,p}}) \quad \text{S5.22}$$

Gas-particle partitioning kinetic can thus be estimated by time scale of gas-phase diffusion and particle-phase diffusion. Particle-phase diffusion characteristic time scale $\tau_{p,i}$ are shown in Equation S5.23:

$$\tau_{p,i} = \frac{d_p^2}{4\pi^2 D_{p,i}} \quad \text{S5.23}$$

For surface processes, adsorption processes of gas-phase molecules are characterized by mass accommodation coefficient α as shown previously in Eqs. 5.10-5.12, while desorption processes are determined by desorption energies. Rate constant of desorption processes $k_{des,i}$ are estimated based on conventional transition state (TS) theory that depends on desorption energy $E^0_{des,i}$, as shown in Equation S5.24:

$$k_{des,i} = A_{des} \cdot \exp(-\frac{E^0_{des}}{T}) \quad \text{S5.24}$$

In Equation S5.24, A_{des} is pre-exponential factor depends on surface transition kinetics, which is set to 10^{13} s^{-1}; $E^0_{des,i}$ are estimated utilizing 2-D-VBS-based parameterization recommended in their articles as shown in Equations S5.24-5.25. In Eqs. S5.25-5.26, $E^0_{des,i}$ depends on O:C ratio and polarizability α_{polar} . Desorption time scale $\tau_{des,i}$ are thus determined to be inverse number of $k_{des,i}$.

$$E^0_{des}(kJ \cdot mol^{-1}) = 25.895 + 2.330\alpha_{polar}(10^{-24}cm^3) + 12.367(O:C) \quad \text{S5.25}$$

$$\alpha_{polar}(10^{-24}cm^3) = 1.51n_C + 0.17n_H + 0.57n_N + 1.05n_O + 2.99n_S \quad \text{S5.26}$$

Comparison between characteristic time scales in kinetic processes including $\tau_{g,i}$, $\tau_{p,i}$

and $\tau_{des,i}$, and reference times gives insight into gas-particle partitioning dynamics in the experiment. Reference time includes retention time in Go:PAM t_R(55s), e-folding oxidation-consumption time of oleic acid τ_{oleic}, and characteristic coagulation time τ_{coag}. Characteristic time of oleic acid oxidation are adapted from EPI SUITE, while characteristic time are generated from SMPS-measured particle size distributions, shown in Equation R5.27. Coagulation coefficients $K_{i,j}$ are determined by aerodynamic properties discussed in detail in Chapter 13.3 of Seinfeld et al..

$$\tau_{coag,i} = \frac{1}{\sum_j K_{i,j} N_i} \qquad \text{S5.27}$$

Kinetic estimation results are shown in Figure 4. The calculations indicate that particle-phase diffusion is the fastest modeled process in both primary and secondary aerosols and is substantially faster than the residence time in the Go: PAM and the oxidation time scale of primary precursors such as oleic acid. Particle-phase diffusion is therefore unlikely to be the dominant resistance under the modeled conditions. Gas-phase diffusion in the primary-aerosol case has a characteristic time scale of approximately 10^2 s because of the low primary particle number concentration, whereas gas-phase diffusion in the secondary-aerosol case remains faster than the oxidation and residence time scales. Surface-desorption time scales increase with molecular weight: compounds with molecular weight >200 g mol^{-1} have desorption times longer than the residence time and account for approximately 10% of the total mass, whereas compounds with molecular weight >300 g mol^{-1} have desorption times longer than 1 h and account for approximately 5% of the total mass. Thus, surface desorption may kinetically retain a limited fraction of high-molecular-weight compounds, while its influence on semi-volatile and intermediate-volatility components remains minor. Varying the mass accommodation coefficient from 1 to 10^{-4} (Figure 4, Figures S6.46-6.47) had only a minor effect on the calculated time scales. Different viscosity parameterizations produced substantial differences in the estimated viscosity and particle-phase diffusion time scales (Figure S6.45), but particle-phase diffusion remained faster than the other modeled processes. Overall, the results indicate that primary aerosols favor vaporization and gas-phase partitioning, whereas secondary aerosols are at or near gas-

particle partitioning equilibrium under the studied OH-exposure range (<10^{10} molecules cm^{-3} s). We therefore no longer attribute the observed behavior primarily to particle-phase diffusion and instead discuss gas-phase transport in the primary-aerosol case and surface desorption of a small high-molecular-weight fraction as possible kinetic limitations.

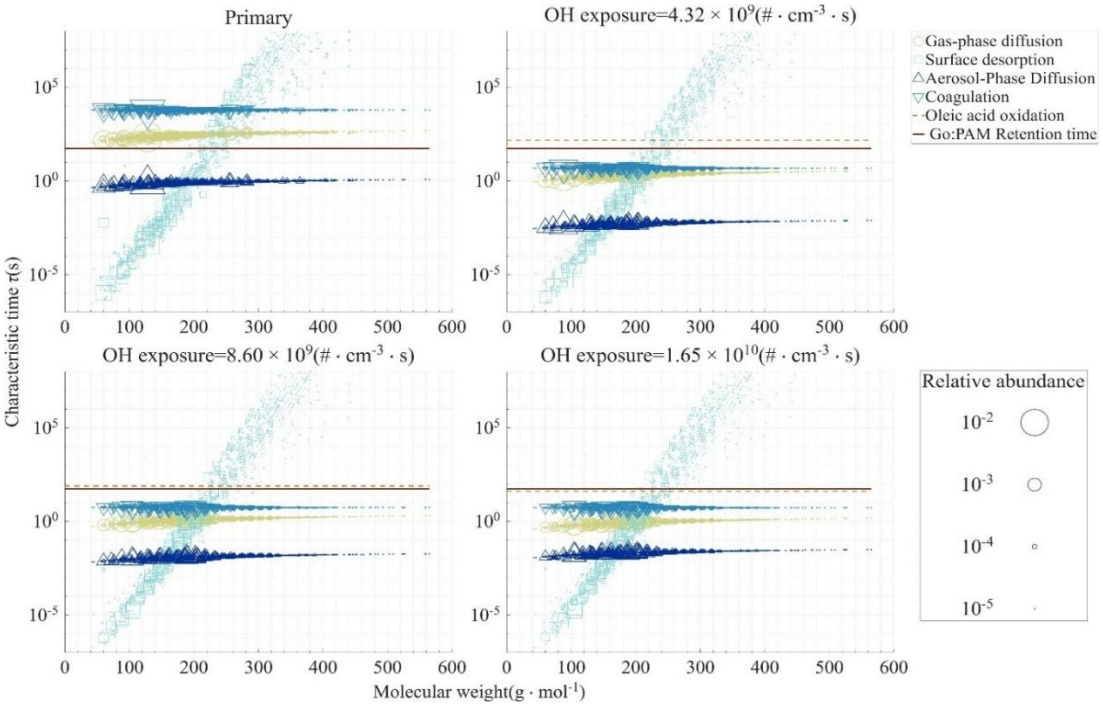

Figure 4 The characteristic time scale of FIGAERO-CIMS detected species in various kinetic transport processes of gas-particle partitioning with enhancement of OH exposure. Markers show time scale of gas-phase diffusion(circle), surface desorption(square), aerosol-phase diffusion(triangle), coagulation (reverse triangle). Lines shows reference time scale, including retention time(solid) and oleic acid oxidation(dashed). Marker size represents relative abundance of species. Surface mass accommodation coefficients are chosen to be unity.

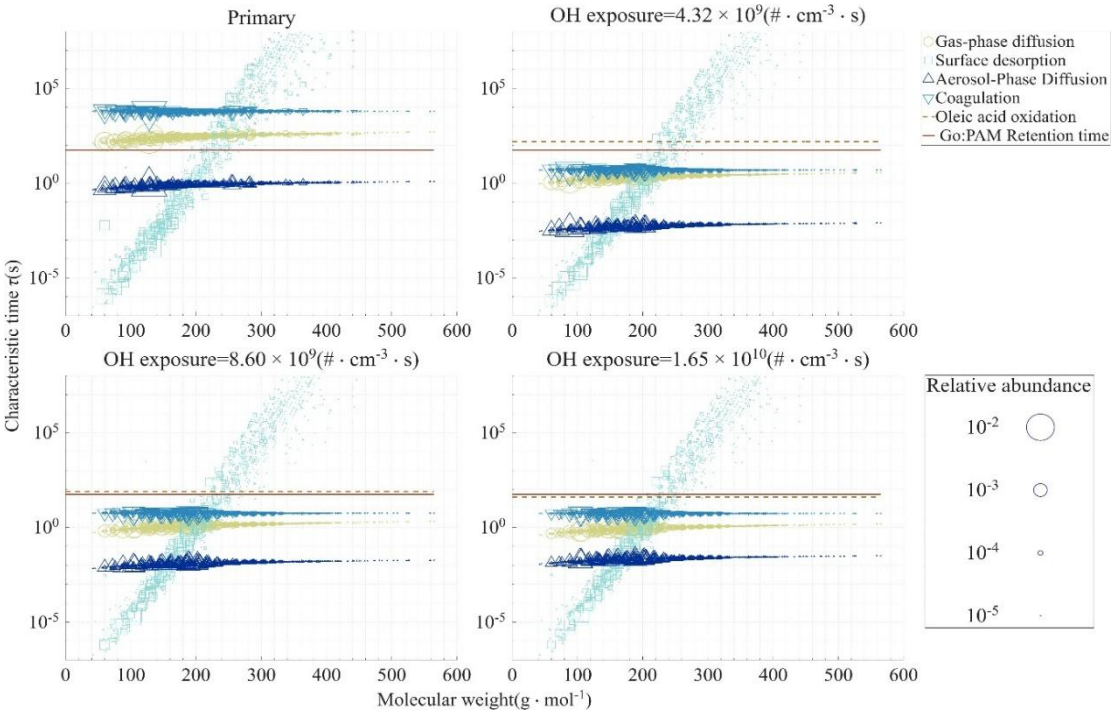

Figure S6.46 Characteristic time scales of FIGAERO-CIMS-detected species for gas-particle partitioning processes across the investigated OH exposures. Markers and lines are defined same as in Figure 4. Surface mass accommodation coefficient $\alpha = 10^{-4}$

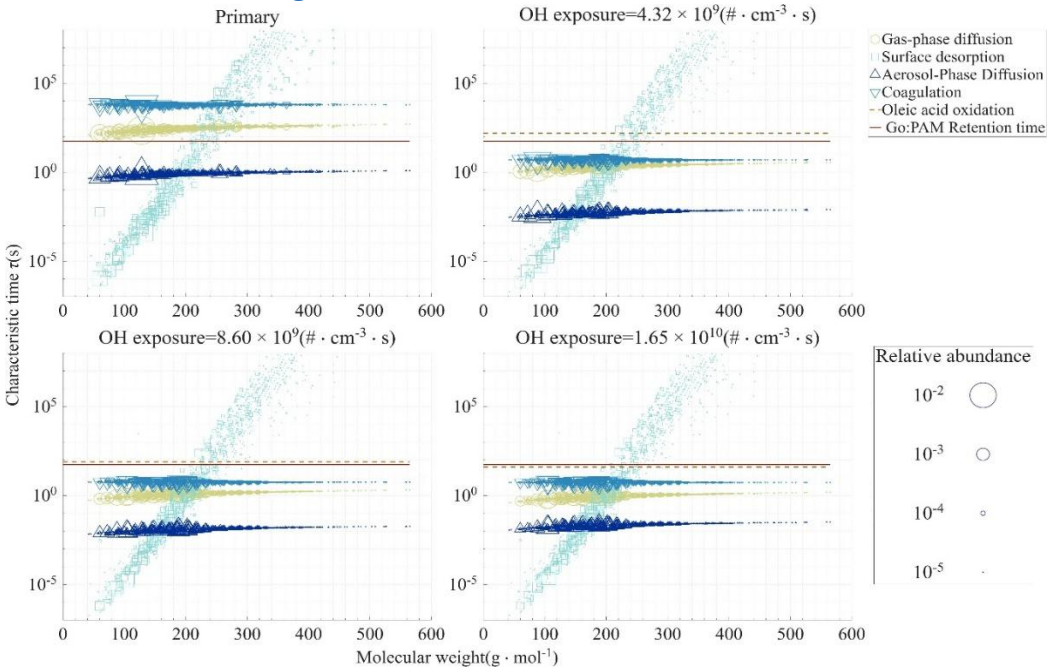

Figure S6.47 Characteristic time scales of FIGAERO-CIMS-detected species for gas-particle partitioning processes across the investigated OH exposures. Markers and lines are defined as in Figure 4. Surface mass accommodation coefficient $\alpha = 0.01$

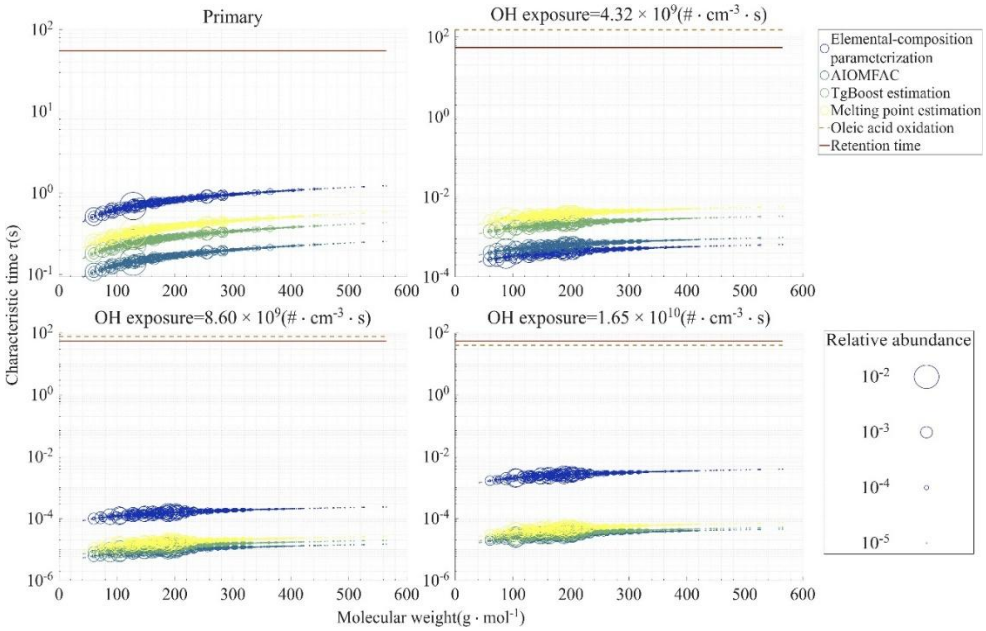

Figure S6.45 Influence of various viscosity estimation method on particle-phase diffusion time scale. Blue: 2-D-VBS based parametrization; blue-green: AIOMFAC-VISC; green: tgBoost method; yellow: melting point method.

Figure 5 compares the estimated and measured volatilities after accounting for the FIGAERO-based volatility estimates, activity coefficients, and the Kelvin effect; background subtraction was performed before the thermodynamic analysis. The calculation also considered liquid-liquid phase separation (LLPS), which was not predicted for the cooking aerosol under the modeled experimental conditions. Volatility derived from the FIGAERO particle-phase fraction and thermogram peak temperature was lower and more narrowly distributed than the theoretical estimates. Sensitivity tests has been bone by adding up long-chain-fatty-acid-related compounds to measurement results with intensity at 10% of total intensities, shown in Figure S6.50-51. Sensitivity test shows minor changes in kinetic and thermodynamic properties after addition, indicating that underestimation of I-CIMS on fatty acids and highly-oxidized compounds would be a minor influence on discrepancies in gas-particle partitioning. Possible explanations include hindered evaporation and desorption caused by the FIGAERO filter microstructure (Ylisirniö et al., doi: 10.5194/amt-15-4385-2022; doi: 10.5194/amt-18-6449-2025), aerosol microstructure associated with functionalized autoxidation products, and uncertainty in activity coefficients (doi: 10.1016/j.atmosres.2025.108464; doi: 10.1021/acs.estlett.4c00608; doi:

10.1038/s41612-025-01156-z). We therefore present this discrepancy as an unresolved measurement-model gap rather than as evidence for a single kinetic mechanism.

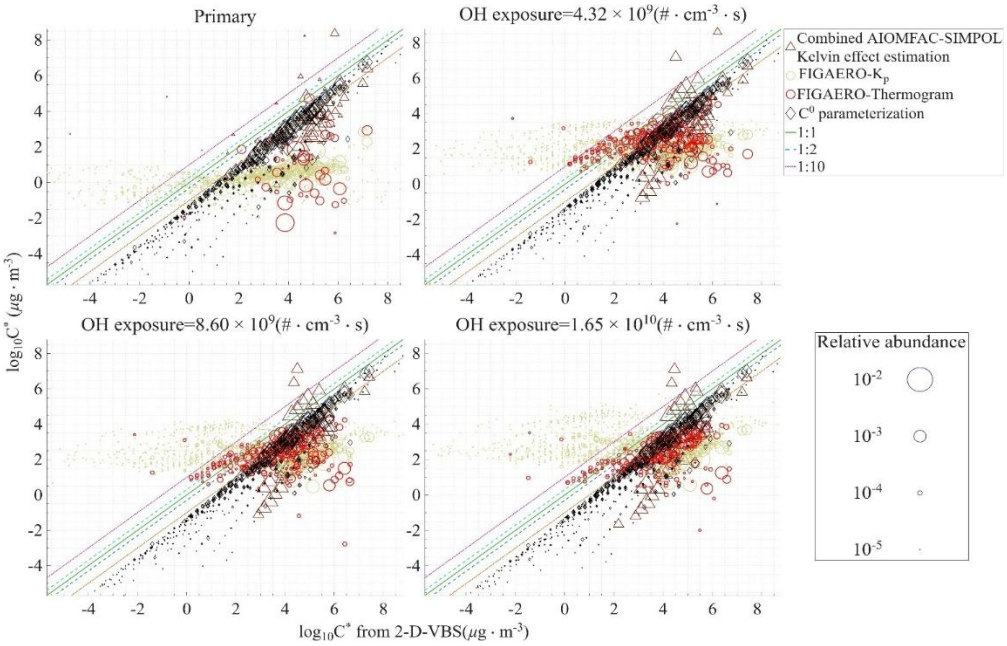

Figure 5 The characteristic effective saturated concentration C^* of FIGAERO-CIMS detected species utilizing different estimation methods with enhancement of OH exposure. Markers show combined AIOMFAC-SIMPOL vapor-pressure and activity coefficient estimation methods accounting for kelvin effect (triangle), K_p from FIGAERO measurements (yellow circle), T_{max} from FIGAERO thermograms (red circle), C^* parametrization (reverse triangle). Lines shows 1:1,1:2 and 1:10 position. Marker size represents relative abundance of species.

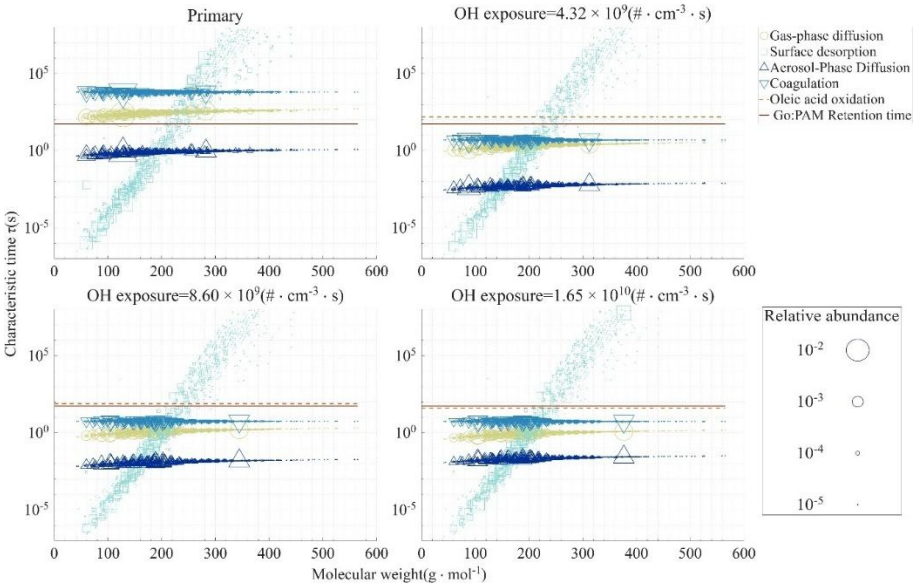

Figure S6.50 Sensitivity analysis on influence of possible underestimated long-chain fatty acid related species on kinetics of FIGAERO-CIMS-detected species for gas-particle partitioning processes across the investigated OH exposures. Markers and lines are defined as in Figure 4. Surface mass accommodation coefficient $\alpha = 1$

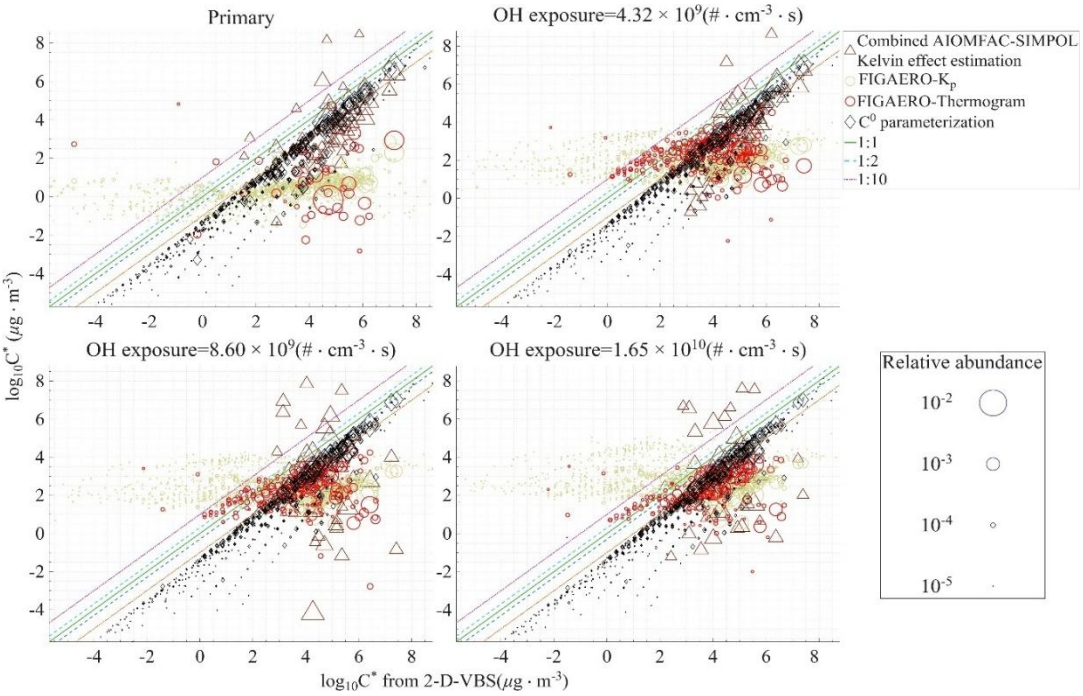

Figure S6.51 Sensitivity analysis on influence of possible underestimated long-chain fatty acid related species on thermodynamics of FIGAERO-CIMS-detected species for gas-particle partitioning processes across the investigated OH exposures. Markers and lines are defined as in Figure 5.

The revised kinetic and thermodynamic discussion in Section 3.4 reads:

"Gas-particle partitioning is governed by both thermodynamic and kinetic processes. Particle-phase diffusion is the fastest modeled process in both primary and secondary aerosols across the investigated OH exposures, with characteristic time scales of approximately 10^{-2}–10^{0} s, substantially shorter than the 55 s residence time and the oxidation time scale of primary precursors. It is therefore unlikely to be the dominant kinetic resistance under the modeled conditions."

"Gas-phase diffusion in the primary aerosol is partly limited by the low particle number concentration and has a characteristic time scale of approximately 10^{2} s. In the secondary aerosol, gas-phase diffusion remains faster than the oxidation and residence time scales. Surface-desorption time scales increase with molecular weight: species with molecular weight >200 g mol^{-1} have desorption times longer than the residence time and account for approximately 10% of the total detected mass, whereas species with molecular weight >300 g mol^{-1} have desorption times longer than 1 h and account for approximately 5%."

"Varying the mass accommodation coefficient from 1 to 10^{-4} has only a minor

effect on the modeled time scales (Figure 4 and Figures S6.46–S6.47). Different viscosity parameterizations produce substantial variation in viscosity and particle-phase diffusion time scales (Figure S6.45), but particle-phase diffusion remains faster than the other modeled processes. Overall, the calculations indicate that the major components of the secondary aerosol are at or near gas-particle partitioning equilibrium under the investigated conditions."

"Volatility derived from the FIGAERO particle-phase fraction and thermogram peak temperature was lower and more narrowly distributed than the theoretical estimates. Possible explanations include hindered evaporation and desorption caused by the FIGAERO filter microstructure, thermal decomposition or rearrangement during desorption, aerosol microstructure, and uncertainty in pure-component vapor pressures and activity coefficients. We therefore treat the discrepancy as an unresolved measurement-model gap rather than evidence for a single kinetic mechanism."

Additional major comments / requests for clarification

1. ***VOCUS-PTR quantification: Please clarify whether and how fragmentation effects and compound-dependent sensitivities were handled for VOCUS-PTR quantification, especially for oxygenated oxidation products. This affects interpretation of precursor decay and product formation.***

Response: For compounds included in the calibration experiments, the VOCUS-PTR data were processed using the measured sensitivities and observed fragmentation. For uncalibrated compounds, fragmentation could not be treated quantitatively and is reported as a source of uncertainty. Following the reviewer's comment, we revised the sensitivity treatment using the parameterization of Sekimoto et al. (2017, doi: 10.1016/j.ijms.2017.04.006) to account for compound-dependent sensitivity and refine the OH-exposure estimate. For detected ions with the same elemental composition as a compound in the standard gas, we used the sensitivity of the corresponding standard. For species with other formulas, sensitivity was estimated from the relationship between proton-transfer rate and instrument sensitivity after accounting for transmission efficiency. The proton-transfer rate was parameterized from molecular polarizability and dipole moment, which were estimated from elemental composition.

We now state explicitly that this procedure does not quantitatively correct fragmentation for compounds without calibration standards. The revised VOCUS-PTR processing is described in Section S2 of Supplement S1. Figure S2.1 shows the sensitivity estimation methodology.

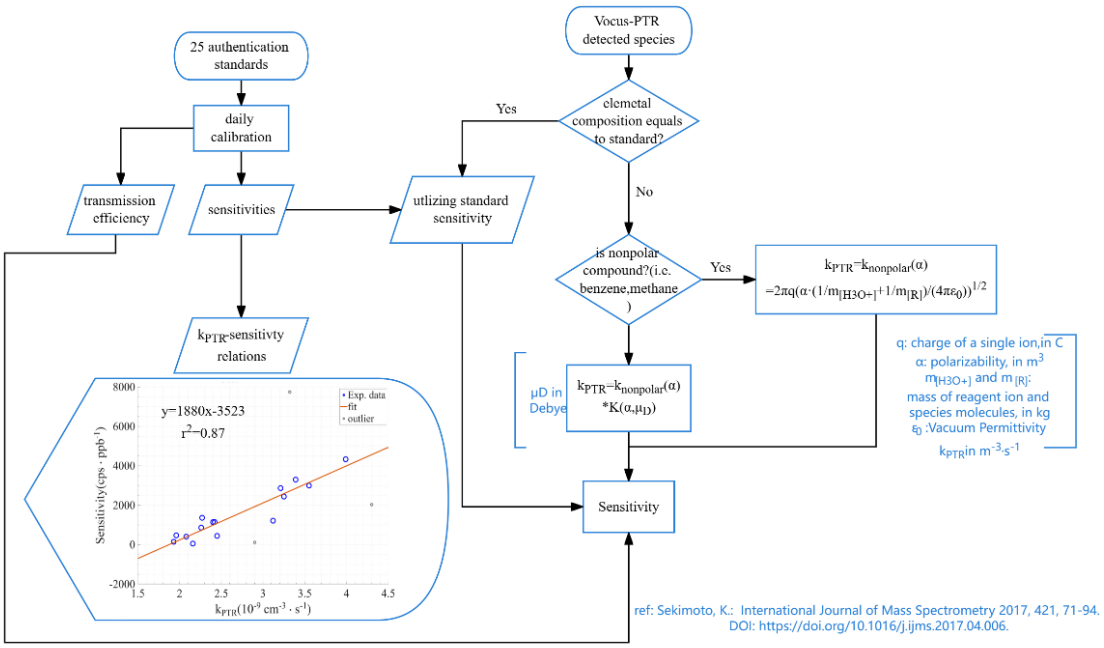

Figure S2.1 Calibration and sensitivity parameterization procedure of Vocus-PTR detected species in this study

The revised VOCUS-PTR quantification description in Section S2 of Supplement S1 reads:

"For compounds included in the calibration experiments, VOCUS-PTR data were processed using the measured sensitivities and observed fragmentation. For detected ions with the same elemental composition as a compound in the standard gas, the sensitivity of the corresponding standard was used. For other formulas, sensitivity was estimated from the relationship between proton-transfer rate and instrument sensitivity after accounting for transmission efficiency. Proton-transfer rates were parameterized from molecular polarizability and dipole moment estimated from elemental composition."

"Fragmentation of species without calibration standards was not treated quantitatively and is therefore retained as a source of measurement uncertainty. The

sensitivity parameterization improves compound-dependent quantification but does not constitute a quantitative fragmentation correction for uncalibrated oxygenated products."

2. ***FIGAERO desorption completeness and background handling: Please clarify whether the authors verified complete desorption under the chosen thermal program for the expected aerosol loadings from cooking emissions (e.g., checks for residual signal, extended desorption tests). Also clarify how background/blank cycles were treated during the experiment and how that influenced the PMF input matrix and uncertainty estimates.***

Response: The FIGAERO-PMF processing is described in Section S4 of Supplement S1. We excluded the first 50 s after switching to particle-phase mode to reduce instrument-switching artifacts, and we estimated the background from the final 40 s of each thermal-desorption period. These processing steps reduce switching and baseline artifacts, but they do not by themselves demonstrate complete desorption at the cooking-aerosol loadings. We therefore do not use the return to the final baseline as proof of complete desorption and treat possible incomplete desorption and carryover as uncertainties in the interpretation of FIGAERO-derived volatility and the PMF results.

The corresponding processing and uncertainty statements in Sections S2 and S4 of Supplement S1 read:

"Before factorization, the first 50 s after switching to particle-phase measurement mode were excluded to reduce potential interference associated with FIGAERO inlet switching. The background term was determined from the average signal during the final 40 s of each thermal-desorption period."

"Excluding the switching interval and subtracting the final-40-s background reduce switching and baseline artifacts, but these steps do not independently demonstrate complete desorption at the experimental aerosol loadings. Possible incomplete desorption and carryover are therefore retained as uncertainties when interpreting FIGAERO-derived volatility and PMF factors."

3. ***Use of "non-targeted" framing: The manuscript frequently frames the approach as non-targeted, yet much of the PMF interpretation relies on identification***

and discussion of specific tracer-like compounds. If the intent is truly non-targeted pattern extraction, more emphasis on bulk/ensemble descriptors (e.g., distributions in carbon number, oxidation state, volatility bins) and how these evolve by factor would be expected, in addition to listing specific ions.

Response: Thank you for this important clarification. In this study, "non-targeted" refers to analysis of the full ensemble of assignable ions rather than a preselected list of tracer compounds. PMF and the 2-D VBS are used to extract ensemble-level patterns in volatility, composition, and oxidation evolution. Representative ions are then used to support factor interpretation, but they are not the sole basis of the analysis and are not treated as unique structural identifications. We revised the manuscript to clarify this definition and to place greater emphasis on bulk and factor-level descriptors.

The methodological framing in Sections 2.2–2.4 has been clarified as follows:

"In this study, 'non-targeted' refers to analysis of the full ensemble of 936 assignable FIGAERO-I-CIMS ions rather than a preselected list of tracer compounds. PMF and the 2-D VBS are used to extract ensemble-level patterns in volatility, composition, and oxidation evolution. Representative ions are subsequently used to support factor interpretation and are not treated as unique structural identifications."

"Iodide-CIMS is selective toward polar and oxygenated compounds and may underrepresent weakly oxygenated or nonpolar material. Accordingly, the molecular-composition and 2-D VBS distributions reported here describe the detectable iodide-CIMS ion ensemble rather than a mass-complete representation of all cooking emissions."

4. ***Volatility in the 2-D VBS framework: Please clarify the volatility assignment strategy used in the main analysis. The manuscript states that saturation vapor concentration is estimated from elemental composition using an empirical parameterization, but FIGAERO also provides desorption-temperature information that is commonly used to infer volatility. If both approaches are used, their roles and consistency should be clearly described, and provide solid reason why Li et al method is used in 2-D VBS scheme instead of experimentally obtained C* data from FIGAERO.***

Response: We clarified the different roles of the 2-D VBS parameterization and the FIGAERO-derived volatility estimates. The Li et al. formula-based parameterization is used to assign C* values consistently across the detected formulas and to support comparison with previous 2-D VBS studies. FIGAERO-derived estimates from Kp and thermograms are used as experimental comparisons rather than as the sole coordinate for the 2-D VBS analysis. As shown in Figure 5and Figures S6.52-55, the FIGAERO-derived volatilities are lower and more narrowly distributed than the theoretical estimates. Because thermogram-derived volatility can be influenced by desorption and filter effects, and because the discrepancy among the approaches remains unresolved (doi: 10.5194/amt-15-4385-2022; doi: 10.5194/acp-23-6613-2023; doi: 10.5194/acp-22-1195-2022), we retained the Li et al. parameterization for the main 2-D VBS intercomparison and discuss the FIGAERO comparison separately in Section 3.4.

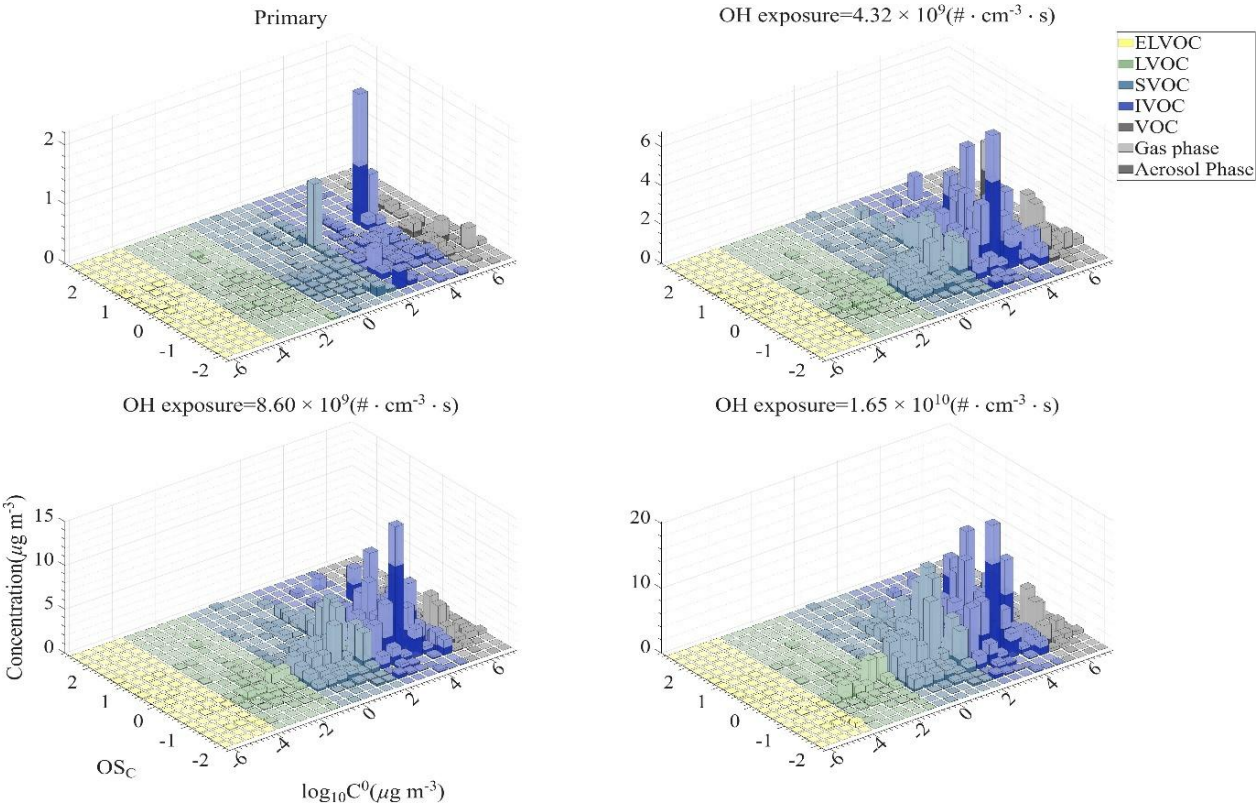

Figure S6.52 Distribution of gas-phase and aerosol-phase primary and secondary cooking organic species in 2-D VBS space with oxidation. The volatility axis is saturated concentration C^0 determined by 2-D-VBS parameterization recommended by Li et al.,2016.

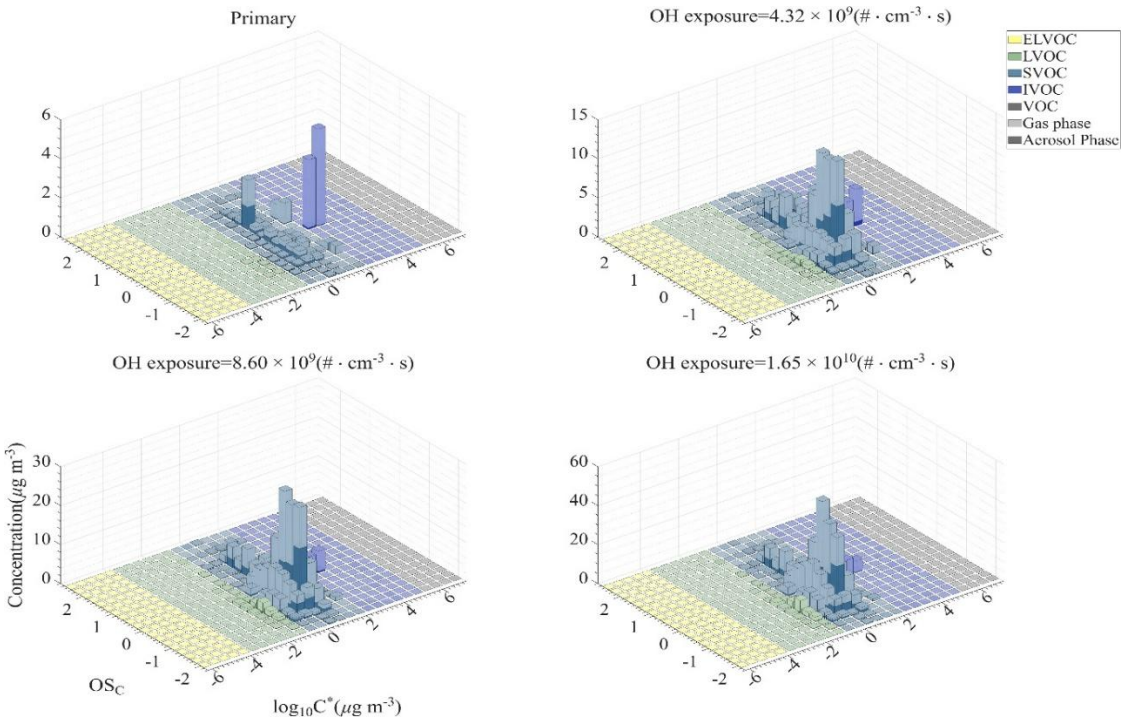

Figure S6.53 Distribution of gas-phase and aerosol-phase primary and secondary cooking organic species in 2-D VBS space with oxidation. The volatility axis is effective saturated concentration C^* determined from gas-phase and particle-phase concentration measured by FIGAERO-CIMS.

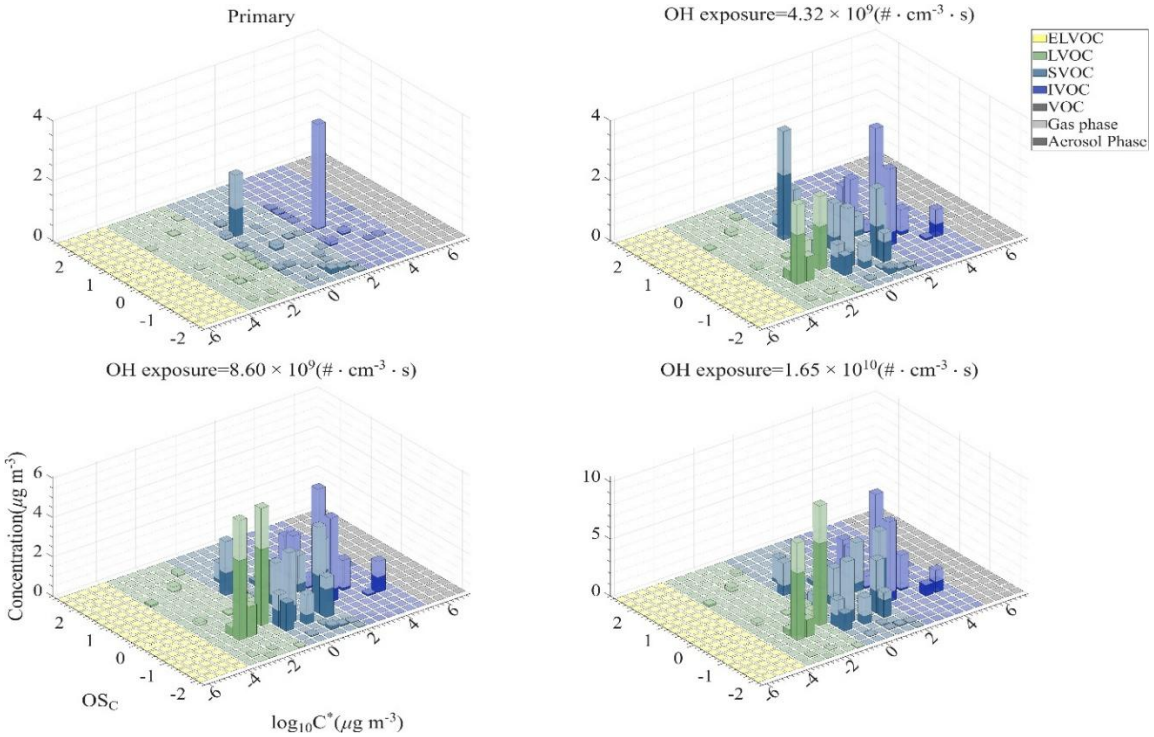

Figure S6.54 Distribution of gas-phase and aerosol-phase primary and secondary cooking organic species in 2-D VBS space with oxidation. The volatility axis is effective saturated concentration C^* determined from thermograms measured by FIGAERO-CIMS.

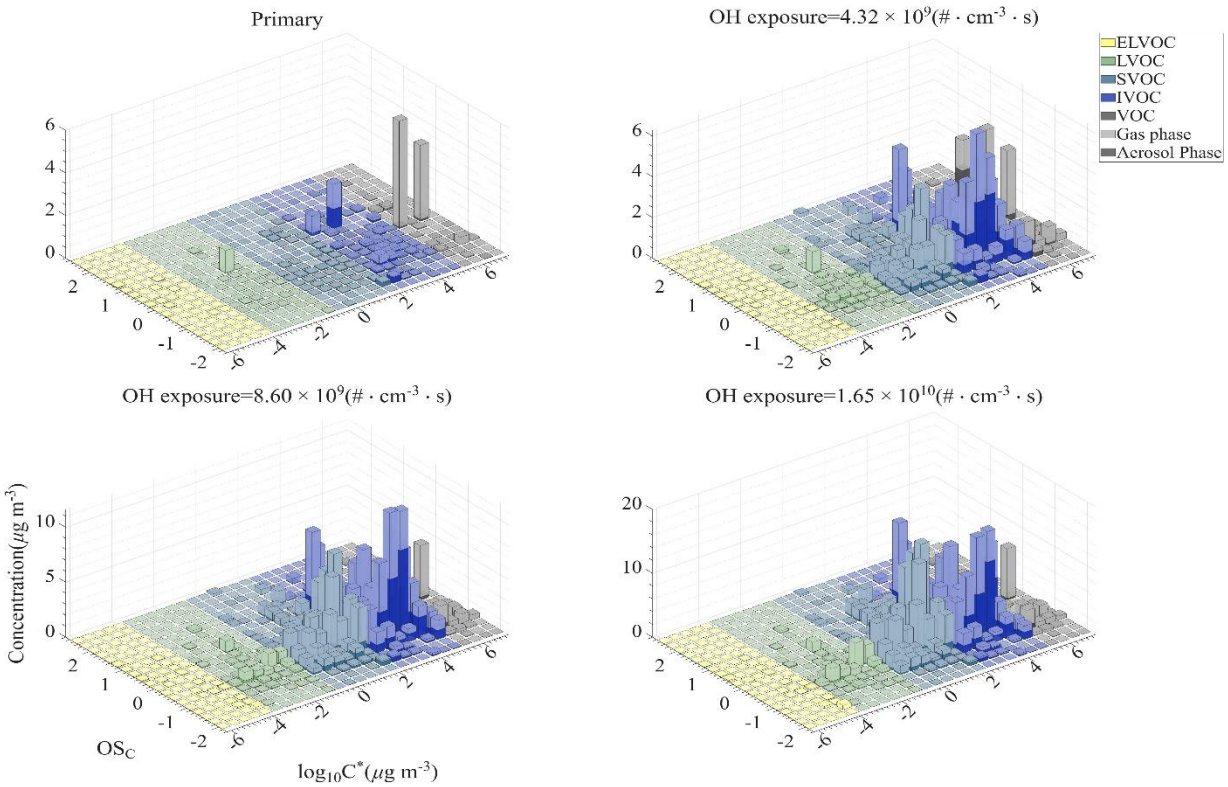

Figure S6.55 Distribution of gas-phase and aerosol-phase primary and secondary cooking organic species in 2-D VBS space with oxidation. The volatility axis is effective saturated concentration C^* determined from vapor pressure estimation from SIMPOL and activity coefficient from AIOMFAC. Kelvin effect is also considered in C^* calculation.

The revised explanation in Sections 2.5 and 3.4 and the associated Supplement captions reads:

"The Li et al. formula-based parameterization is used to assign C values consistently across the detected formulas and to support comparison with previous 2-D VBS studies. FIGAERO-derived estimates from Kp and thermograms are used as experimental comparisons rather than as the sole volatility coordinate for the 2-D VBS analysis."*

"Experimental Kp values are derived from paired FIGAERO gas- and particle-phase measurements together with the measured organic-aerosol mass concentration. For the equilibrium calculation, the organic mass fraction is assumed to be unity, the mean particle-phase molecular weight is calculated as an abundance-weighted value for the detected composition, activity coefficients are calculated with AIOMFAC, and a surface tension of 0.05 N m^{-1} is used for the Kelvin correction."

"Figures S6.50–S6.53 compare 2-D VBS representations based on the Li et al.

parameterization, FIGAERO gas- and particle-phase concentrations, FIGAERO thermograms, and the combined SIMPOL-AIOMFAC-Kelvin treatment. The FIGAERO-derived volatilities are lower and more narrowly distributed than the theoretical estimates; this discrepancy is discussed separately rather than being used to redefine the primary 2-D VBS coordinate."

5. ***Figure 1 / Section 3.1 clarity: In Section 3.1 and Figure 1, the evidence for new particle formation and condensational growth should be apparent from the increase in number concentration and the evolution of the size distribution. However, I found the current discussion somewhat difficult to follow and potentially internally inconsistent across panels. Specifically, if Figure 1a–b represent the primary aerosol size/mass distributions from cooking, I would expect these to closely resemble the lowest-OH-exposure cases shown in Figure 1c–d (i.e., near-zero oxidation). As presented, it is not clear to me how the "primary" distributions in 1a–b relate to the baseline conditions in 1c–d, or how the transition from primary to secondary distributions is defined in the plotting and analysis. Please clarify (i) what dataset/conditions are used for the "primary" panels, (ii) what OH-exposure case corresponds to the unoxidized baseline in 1c–d, and (iii) how the authors separate primary vs secondary modes across the figure.***

Response: We revised Section 3.1 and the Figure 1 caption to clarify the datasets and the distinction between the primary and secondary modes. Panels (a)-(b) show the primary cooking-aerosol size and mass distributions, whereas panels (c)-(d) show the secondary-aerosol distributions measured over OH exposures of 0.1-1.8 x 10^{10} molecules cm^{-3} s. Thus, the lowest-OH case in panels (c)-(d) is the lowest oxidized reactor condition and is not the same dataset as the primary panels. We define the primary mode as the broad 50-300 nm distribution and the secondary mode as the predominantly monomodal nanoparticle distribution below 50 nm. Even at the lowest OH exposure, the secondary particle number concentration reached approximately 10^{6} cm^{-3}. As OH exposure increased from approximately 10^{9} to 10^{10} molecules cm^{-3} s, the secondary mode diameter increased from 14.1 to 31.1 nm, while the total number

concentration increased from 1.37 × 10^6 to 3.42 × 10^6 cm^{-3}. This indicates that the increase in SOA mass at higher OH exposure was driven predominantly by particle growth rather than by a proportional increase in particle number. Particles larger than 90 nm show minimal changes in number and mass concentration by less than 20% on average even at the highest OH exposure (Figure S6.1). These observations support nucleation and condensation of gas-phase oxidation products as the main source of the secondary mode rather than oxidative aging of the primary particles and coagulation of existing particles. The possible role of limited miscibility between the less-polar primary components and more polar secondary products is indirectly corroborated by only slight concentration decrease of long-chain fatty acid (Figures S6.9, 6.10), while still retained as a proposed explanation. (Rogge et al., 1991; Nolte et al., 1999)

The revised description in Section 3.1 and the Figure 1 caption reads:

"Primary cooking aerosols exhibit a broad size distribution, with particle diameters of approximately 50–300 nm. In contrast, the secondary organic aerosol is dominated by a monomodal nanoparticle population below 50 nm. Even at the lowest OH exposure, the secondary particle number concentration reaches approximately 10^6 cm^{-3}. As OH exposure increases from approximately 10^9 to 10^{10} molecules cm^{-3} s, the secondary mode diameter increases from 14.1 to 31.1 nm, while the total number concentration increases from 1.37 × 10^6 to 3.42 × 10^6 cm^{-3}."

"Figure 1. Evolution of the primary and secondary aerosol size and mass distributions with increasing OH exposure. Panels (a) and (b) show the size and mass distributions of the unoxidized primary aerosol. Panels (c) and (d) show the size and mass distributions of the secondary aerosol across OH exposures of 0.1–1.8 × 10^{10} molecules cm^{-3} s. Panel (e) shows the evolution of aerosol mass concentration from the primary condition to the highest OH exposure."

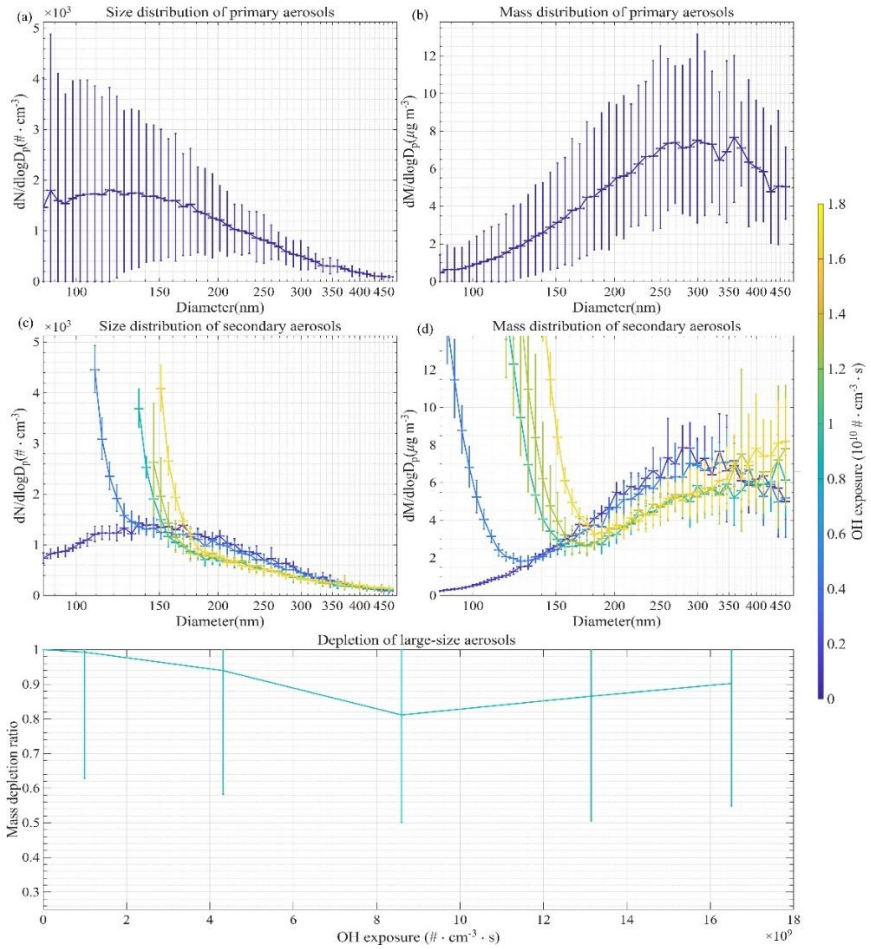

Figure S6.1 Primary and secondary aerosol size & mass distribution evolution at diameter >90nm with OH exposure growth from 0.1~1.8×10^{10} #·cm^{-3}·s during oxidation experiments. (a) number distribution, (b) mass distribution of primary aerosols; (c) (d) size and mass distribution of secondary aerosols, (e) total mass shrinking ratio of aerosols after oxidation in Go:PAM flow tube

6. ***Temporal evolution evidence for multi-generation products: Several statements about multi-generation oxidation products and their volatility class (IVOC/SVOC) would be strengthened by clearer presentation of temporal evolution (or oxidation-age-resolved) behavior of representative compound classes and/or factor contributions.***

Response: We classified the multi-generation products using both molecular composition and their evolution with OH exposure. $C_{18}H_{32}O_6$ is assigned as a possible autoxidation product that retains a long-chain fatty-acid structure, whereas $C_{10}H_{18}O_5$ may correspond to a hydroxy C_{10} diacid or a hydroperoxide. Both increase rapidly with

OH exposure and reach higher oxidation states, while the related lower-oxygen homologues $C_{18}H_{32}O_4$ and $C_{10}H_{18}O_4$ increase more slowly or decrease after a certain OH exposure. We therefore describe these compounds as possible or putative multi-generation products rather than as unique structural identifications. Concentration evolution of species mentioned above are shown in Figure S6.36-6.38 and Figure R1, proposed thermal and OH-oxidation pathways are summarized in Figure S6.56.

The revised interpretation and associated mechanism figure description reads:

"The multi-generation factors reach their highest abundance at the highest experimental OH exposures. C18H32O6 is assigned as a possible autoxidation product that retains a long-chain fatty-acid structure, whereas C10H18O5 may correspond to a hydroxy C10 diacid or a hydroperoxide. Both increase rapidly with OH exposure, while the related lower-oxygen homologues C18H32O4 and C10H18O4 increase more slowly or decrease after a certain exposure. These assignments are therefore described as possible or putative structures rather than unique molecular identifications."

"Figure S6.54 summarizes the proposed thermal-decomposition and atmospheric-oxidation pathways of cooking-oil components, including glycerol-related compounds and long-chain-fatty-acid-related compounds. The scheme is used to organize the observed molecular and factor-evolution patterns rather than to claim unique structures for individual molecular formulas."

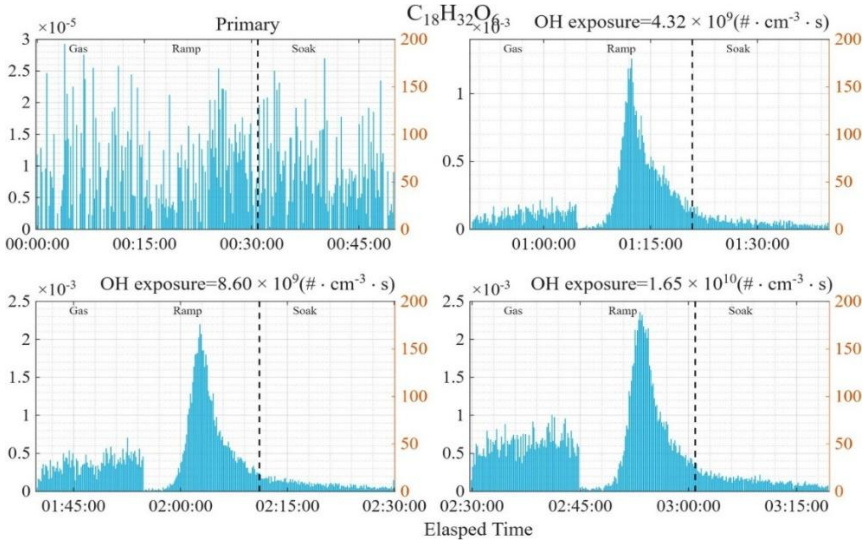

Figure S6.36 Concentration time series of compound with elemental composition of $C_{18}H_{32}O_6$ at different OH exposure during FIGAERO measurement of flow tube experiment.

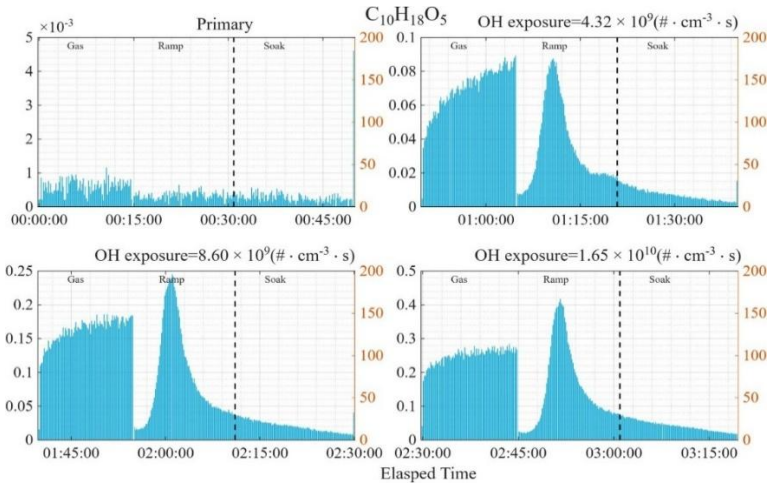

Figure S6.37 Concentration time series of compound with elemental composition of $C_{10}H_{18}O_5$ at different OH exposure during FIGAERO measurement of flow tube experiment.

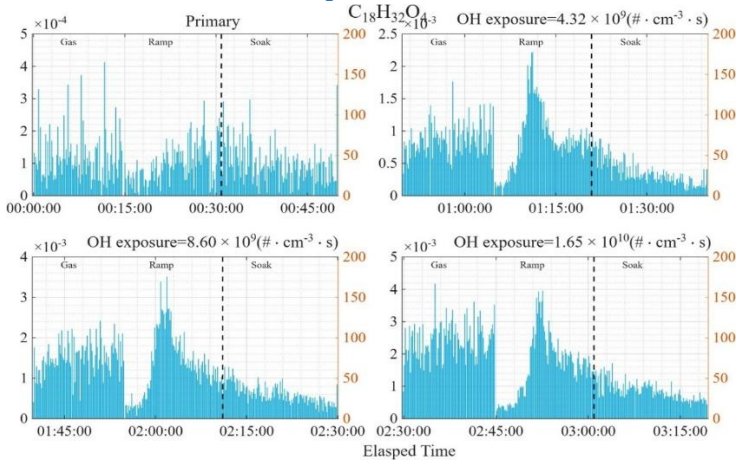

Figure R1 Concentration time series of compound with elemental composition of $C_{18}H_{32}O_4$ at different OH exposure during FIGAERO measurement of flow tube experiment.

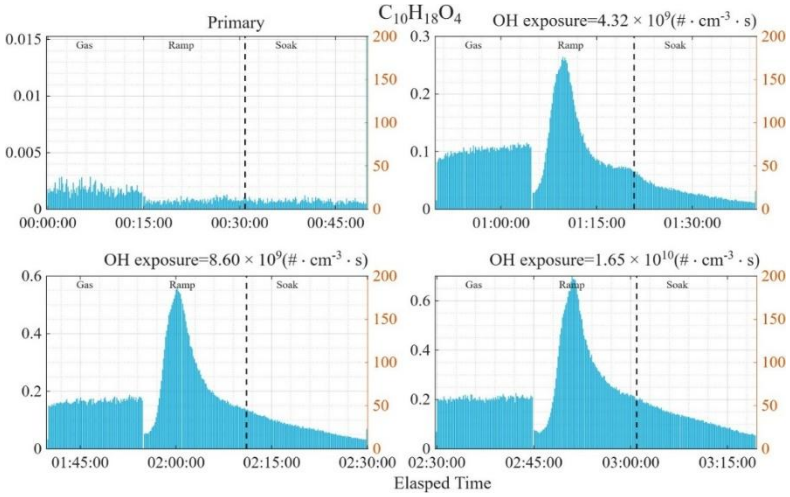

Figure S6.38 Concentration time series of compound with elemental composition of $C_{10}H_{18}O_4$ at different OH exposure during FIGAERO measurement of flow tube experiment.

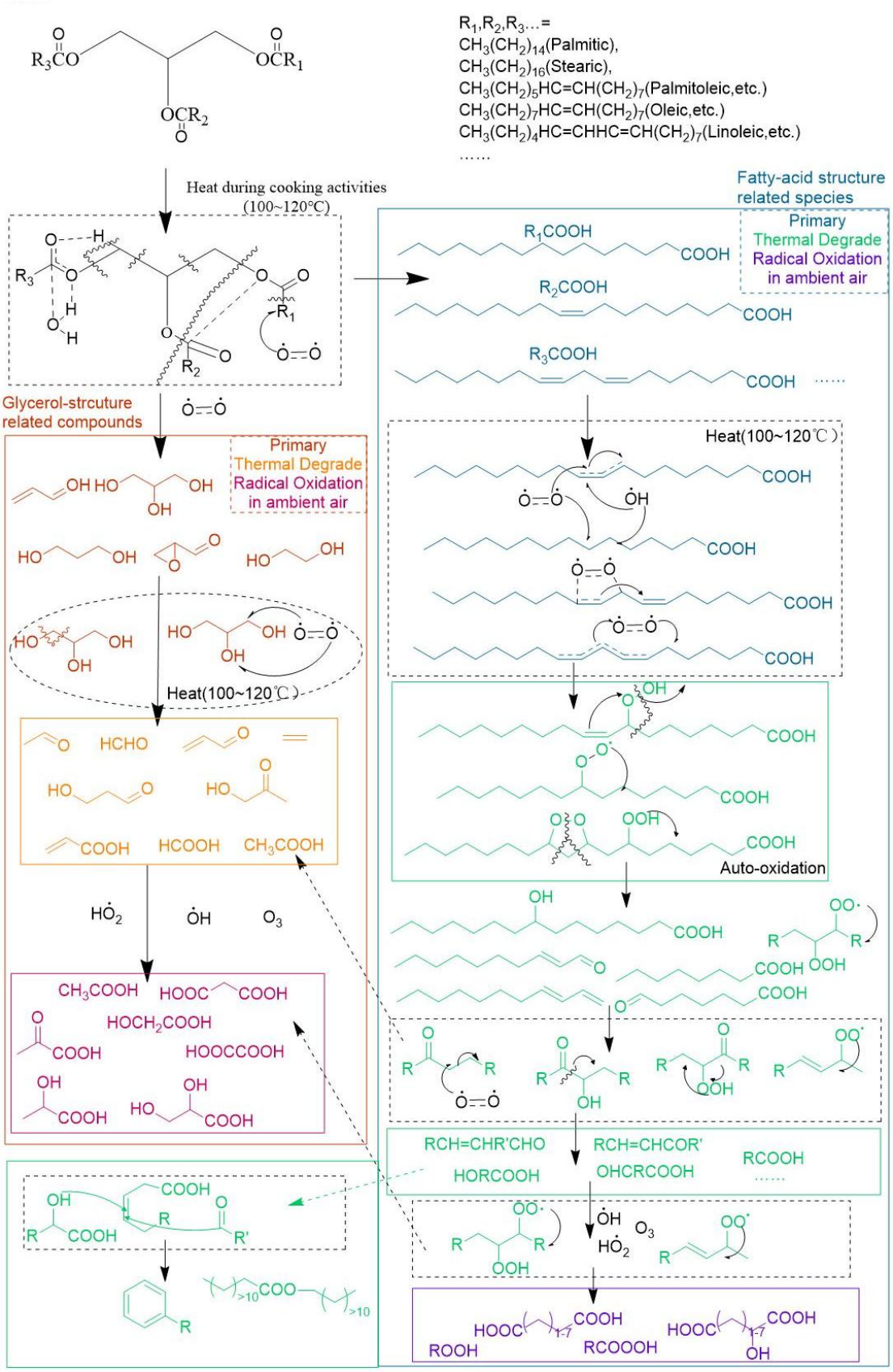

Figure R29 Thermal decomposition and oxidation mechanism of fat during cooking process and in ambient air.

7. ***Nucleation mechanism vs. volatility class: The manuscript emphasizes growth in IVOC/SVOC material in the 2-D VBS framework. Please reconcile this with expectations for new particle formation pathways (often associated with low-volatility/ELVOC material), or clarify the nucleation/condensation mechanism implied by the observations.***

Response: We revised Sections 3.1 and 3.4 to distinguish initial particle formation from subsequent particle growth. The appearance of particles at low OH exposure is consistent with nucleation involving a small fraction of low-volatility oxidation products, whereas the increase in particle diameter and mass at higher OH exposure can be explained by condensation of the more abundant SVOC/IVOC material onto newly formed and pre-existing particles. Because the present measurements do not directly resolve the molecular clusters responsible for nucleation, we now present the nucleation mechanism as a plausible interpretation rather than as a uniquely demonstrated pathway.

The revised discussion distinguishing particle formation and subsequent growth reads:

"The appearance of nanoparticles at the lowest OH exposure is consistent with initial particle formation involving a small fraction of low-volatility oxidation products. Because the measurements do not directly resolve the molecular clusters responsible for nucleation, this pathway is presented as a plausible interpretation rather than a uniquely demonstrated mechanism."

"At higher OH exposures, the increase in mode diameter from 14.1 to 31.1 nm and the increase in aerosol mass are attributed primarily to condensation of the more abundant SVOC/IVOC material onto newly formed and pre-existing particles. Particles larger than 90 nm change by less than 20% on average even at the highest exposure, indicating that oxidative aging of the original primary-particle mode and coagulation are not the dominant explanations for the observed secondary mode."

8. ***Presentation and internal consistency (figures): The figures are often difficult to interpret quickly (labels/fonts/organization), and some figure citations appear inconsistent with the figure numbering/labels. Please ensure that all figure***

references in the text match the correct figures (including the Supplement), and revise figure labeling for readability.

Response: Thank you for pointing this out. We checked the main-text and supplementary figure labels, panel descriptions, numbering, and cross-references, and revised the inconsistent labels and citations. No plotted data were changed.

Examples of revised captions and cross-references include:

"Figure 4. Characteristic time scales of FIGAERO-I-CIMS-detected species for gas-phase diffusion, surface desorption, particle-phase diffusion, and coagulation across the investigated OH exposures. The residence time and oleic-acid oxidation time scale are shown as references; marker size represents relative abundance."

"Figure 5. Effective saturation concentrations derived using the SIMPOL-AIOMFAC-Kelvin treatment, FIGAERO gas-particle partitioning, FIGAERO thermogram peak temperature, and the formula-based 2-D VBS parameterization. The 1:1, 1:2, and 1:10 reference lines are shown for comparison."

"Supplementary cross-references were checked against the expanded figure sequence. The accommodation-coefficient sensitivity analysis is cited as Figures S6.46–S6.47, the volatility and 2-D VBS comparison as Figures S6.48–S6.53, and the proposed thermal and oxidation mechanism as Figure S6.54."